INTERNATIONAL JOURNAL OF STRUCTURAL CHANGES IN SOLIDS – Mechanics and Applications
Volume 1, Number 1, December 2009, pp. 83-109

IJSCS

Smooth Conformal α-NEM for Gradient Elasticity

A. Rajagopal[a], M. Scherer[a], P. Steinmann[a,*], N. Sukumar[b]

[a] *Chair of Applied Mechanics, University of Erlangen-Nuremberg, Eagerlandstraße 5, D-91058 Erlangen, Germany.*
[b] *Department of Civil and Environmental Engineering, University of California, One Shields Avenue, Davis, CA 95616 USA.*

Abstract

Strain gradient theory for continuum analysis has kinematic relations, which include terms from second gradients of the deformation map. This results in balance equations that have fourth order spatial derivatives, supplemented with higher order boundary conditions. The weak formulation of fourth order operators stipulate that the basis functions must be globally C^1 continuous; very few finite elements in two dimensions meet this requirement. In this paper, we propose a meshfree methodology for the analysis of gradient continua using a conformal α-shape based natural element method (NEM). The conformal α-NEM allows the construction of models entirely in terms of nodes, and ensures quadratic precision of the interpolant over convex and non-convex boundaries. Smooth natural neighbor interpolants are achieved by a transformation of Farin's C^1 interpolant, which are obtained by embedding Sibson's natural neighbor coordinates in the Bernstein-Bézier surface representation of a cubic simplex. Numerical examples are presented to demonstrate the accuracy and efficiency of the proposed method.

1. Introduction

It is well-known that inhomogeneities present in any material at the microscopic scale influence its properties at the macroscopic scale: materials such as suspensions, blood flows, liquid crystals, porous media, polymeric substances, solids with microcracks, dislocations, turbulent fluids with vortices, and composites point to the need for incorporating micro motions in continuum mechanical formulations. There has been considerable focus towards the development of gradient continuum theories that account for the inherent microstructure in such natural and engineering materials. The notion of generalized continua unifies several extended continuum theories that account for such a size dependence due to the underlying microstructure of the material. These can be categorized as gradient continuum theories (see Mindlin and Tiersten (1962), Mindlin (1965), Mindlin and Tiersten (1964)), micro continuum theories (see Eringen (1964), Eringen (1970) and Hirschberger and Steinmann (2007)), and nonlocal continuum theories. In gradient continuum theory, on associating tensors of various order with material points, higher order theories can be constructed (see Eringen (1998), Eringen (1992)).
In this paper, the focus is on developing a computational methodology for solving a gradient continuum formulation. In particular, we consider the strain gradient theory, or the gradient continuum as for example the *second gradient of strain* model as given by Toupin (1962) and Mindlin (Mindlin and Tiersten (1962), Mindlin (1965), Mindlin and Tiersten (1964)). Strain gradient theory requires no additional degrees of freedom but imposes C^1 continuity requirements. A comparison of various higher order gradient theories can be found in Fleck and

*Corresponding author
Email address: paul.steinmann@ltm.uni-erlangen.de (P. Steinmann)

Hutchinson (1996). The present work draws from the contribution of Kirchner and Steinmann (2007), where the variational concepts on gradient and micromorphic continuum have been presented. A more detailed formulation of a gradient approach in spatial and material setting appears in Kirchner and Steinmann (2005) and in Sunyk and Steinmann (2003). The balance equations for a gradient continuum have fourth order spatial derivatives analogous to the biharmonic equation of Kirchhoff plates together with higher order boundary conditions. The solution of these equations require that the primary variable be C^1 continuous; only a few two dimensional finite elements that have been developed for plate bending problems meet this requirement. The most common way for gradient continuum analysis has been through the use of mixed formulations using finite elements (Shu *et al.* (1999), Amanatdou and Aravas (2002)), that only requires C^0 continuity (see Kouznetsova (2002) and Kouznetsova *et al.* (2004)). All these methods lead to extra degrees of freedom in addition to the primary unknowns. The formulation of C^1 finite elements has significant complexity (Stogner and Carey (2007)). An alternative choice with higher order approximants is the use of a meshfree method like the element-free Galerkin (Belytschko *et al.* (1994), Askes and Aifantis (2002)) or the meshless local Petrov Galerkin (see Tang *et al.* (2003)). Most of these methods are for small strains and they pose difficulties in the imposition of boundary conditions because of the non-interpolating property of the approximant.

The natural element method (NEM), which is based on Sibson's C^0 interpolant (Sibson, 1980, 1981) was proposed by Braun and Sambridge (1995). It was used for data approximation in geophysical applications (Sambridge *et al.*, 1995), and also successfully explored for solid mechanics problems by Sukumar *et al.* (1998). Farin proposed a C^1 natural neighbor interpolant (Farin, 1990), which was used by Sukumar and Moran (1999) to solve fourth-order elliptic boundary-value problems. Farin's C^1 interpolant is obtained by embedding Sibson's natural neighbor coordinates in the Bernstein-Bézier surface representation of a cubic simplex (see Farin (1986)), and the transformation adopted by Sukumar and Moran (1999) led to interpolation of nodal function and nodal gradient values. The interpolation property makes the C^1 NEM a suitable candidate for use in the Galerkin implementation of gradient continua. The α-shape based extension of NEM by Cueto *et al.* (2002) enabled the construction of models entirely in terms of nodes and the imposition of essential boundary conditions on non-convex parts of the boundary (Cueto *et al.* (2000)). The use of a conformal α- shapes (Cazals *et al.* (2006)), helps in recovering the whole domain from a discrete set of nodes.

In this paper, a methodolgy for solving a gradient continuum formulation is presented. The kinematics are presented for finite deformations, which include the first and second order gradient terms. For conservative static problems, the Dirichlet principle results in the Euler-Lagrange equations, i.e., the balance of momentum in its strong form. Thus, upon the definition of proper gradient elasticity kinematics, in terms of incorporation of the higher order deformation gradient contribution, a variation of the potential energy renders the weak form of the balance of the momentum together with Neumann boundary conditions and higher order boundary conditions in terms of double force terms. A solution to these equations is presented through the C^1 conformal α-natural element method.

The remainder of this paper is organized as follows. In the next section, we present the kinematics of gradient continua for a geometrically nonlinear setting and the constitutive formulation that includes the length scale effects in the energy expression. Natural neighbor interpolation is introduced in Section 3 and the trial and test approximations used in the C^1 NEM for gradient elasticity are presented in Section 4. The extension to a conformal α-shape based natural element method follows thereafter in Section 5. In Section 6, several numerical examples are presented to demonstrate the accuracy of the method, and we close with a few concluding remarks in Section 7.

2. Gradient Continua

2.1. Kinematic relations

To investigate the variational principle in a geometrically nonlinear setting we refer all quantities arising in the continuum mechanical description to the material configuration $\mathcal{B}_0 \subset \Re^3$ with boundary $\partial\mathcal{B}_0$ and outward unit normal vector $\boldsymbol{N}$. In defining the motion of $\mathcal{B}_0$ a typical continuum particle occupies a succession of points

which for a fixed material point $\boldsymbol{X}$, forms the spatial path for this continuum particle. The position vectors of particles in $\mathcal{B}_0$ are given by $\boldsymbol{X}$, and the nonlinear deformation map

$$\boldsymbol{\varphi} : \mathcal{B}_0 \mapsto \mathcal{B}_t \tag{1a}$$

$$\boldsymbol{X} \mapsto \boldsymbol{\varphi}(\boldsymbol{X}) = \boldsymbol{x} \tag{1b}$$

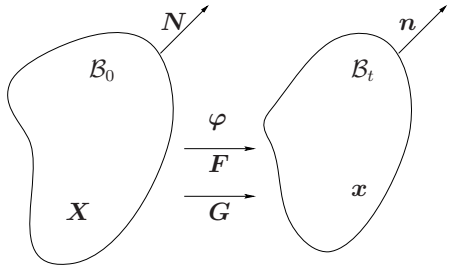

Figure 1: Gradient continuum deformation map

is such that it maps particles $\boldsymbol{X}$ of the material configuration to particles $\boldsymbol{x}$ in the spatial configuration $\mathcal{B}_t$. As usual $\boldsymbol{\varphi}$ is assumed to be sufficiently smooth (C^1 continuous) so that we define the deformation gradient[1]

$$\boldsymbol{F} := \nabla_X \boldsymbol{\varphi}, \;\; F_{iA} := \frac{\partial \varphi_i}{\partial X_A}, \tag{2}$$

where we use small and capital indices to denote the spatial and the material configurations, respectively. The gradient of the deformation map is given by

$$\boldsymbol{G} := \nabla_X \boldsymbol{F} = \nabla_X \nabla_X \boldsymbol{\varphi}, \quad G_{iAB} = F_{iA,B} = \frac{\partial^2 \varphi_i}{\partial X_A \partial X_B}. \tag{3}$$

It is observed that $\boldsymbol{F}$ and $\boldsymbol{G}$ are so-called second and third order two point tensors respectively. Naturally, $\boldsymbol{F}$ does not exhibit any symmetries, but $\boldsymbol{G}$ is symmetric in the last two indices, i.e., for $\boldsymbol{\varphi} \in C^k, k \geq 1$, $G_{iAB} = G_{iBA}$, which follows due to the interchangeability of second-order partial derivatives. The Jacobian determinant is denoted by $J := \det \boldsymbol{F} = dv/dV > 0$, with dV and dv being the infinitesimal volume elements in the material and spatial configurations, respectively.

2.2. Energy considerations and Balance relations

With the above definitions, we turn now to the statement of the underlying Dirichlet problem for gradient continua in the large strain regime using a variational formulation. It is desired to deduce the Euler-Lagrange equations governing gradient continua from the Dirichlet principle given in the form (α is a small, real, scalar-valued parameter)

$$\delta \Pi(\{\bullet\}) = \frac{d}{d\alpha} \left(\Pi(\{\bullet\} + \alpha \delta\{\bullet\}) \right)|_{\alpha=0} \stackrel{!}{=} 0. \tag{4}$$

We consider a gradient continuum for which the potential energy Π is a functional of the deformation, $\boldsymbol{\varphi}$, whereas the stored energy density W_0 depends on $\boldsymbol{F}$ and $\boldsymbol{G}$, so that the functional is written as

$$\Pi(\boldsymbol{\varphi}) = \int_{\mathcal{B}_0} W_0(\boldsymbol{F}, \boldsymbol{G})\, dV + \Pi^{ext}(\boldsymbol{\varphi}). \tag{5}$$

[1]The gradient of any physical quantity, say $\{\circ\}$ with respect to an argument $\{\bullet\}$ for a fixed material placement is denoted by $\nabla_{\{\bullet\}}\{\circ\} = \frac{\partial\{\circ\}}{\partial\{\bullet\}}$.

If we assume the material to be hyperelastic, stresses can be defined as the derivatives of W_0 with respect to their energetically conjugate deformation variables. The macro-stress $\boldsymbol{P}$, and the double stress $\boldsymbol{Q}$ of Piola type together with the volume force density $\boldsymbol{b}_0$ are obtained by the derivatives[2]

$$\boldsymbol{P} := D_F W_0, \quad \boldsymbol{Q} := D_G W_0, \quad \boldsymbol{b}_0 := D_\varphi W_0 \tag{6}$$

For arbitrary variations of $\delta\boldsymbol{\varphi}$, the energy minimization takes the form[3]

$$\delta\Pi = \int\limits_{\mathcal{B}_0} \Big[\boldsymbol{P} : \delta\boldsymbol{F} + \boldsymbol{Q}\vdots\delta\boldsymbol{G} \Big] dV + \delta\Pi^{ext} = 0, \tag{7}$$

where

$$\Pi^{ext} := -\int\limits_{\mathcal{B}_0} \boldsymbol{b}_0 \cdot \boldsymbol{\varphi} dV - \int\limits_{\partial\mathcal{B}_0} \boldsymbol{\varphi} \cdot \boldsymbol{t}_0^P dA - \int\limits_{\partial\mathcal{B}_0} \nabla_X^{(N)} \boldsymbol{\varphi} \cdot \boldsymbol{t}_0^Q dA. \tag{8}$$

In the above equation, $\boldsymbol{b}_0$ is the body force density acting on the material domain $\mathcal{B}_0$. $\boldsymbol{t}_0^P$ and $\boldsymbol{t}_0^Q$ are the nominal surface traction and second-order stress traction, respectively, which act on the surface in the material configuration $\partial\mathcal{B}_0$ (see Mindlin (1965)). By application of Gauss's theorem, we derive the higher order equilibrium equations and Neumann type boundary conditions[4]

$$\mathrm{Div}\,(\boldsymbol{P} - \mathrm{Div}\,\boldsymbol{Q}) = -\boldsymbol{b}_0 \quad \text{in } \mathcal{B}_0 \tag{9}$$

$$[\boldsymbol{P} - \mathrm{Div}\,\boldsymbol{Q}] \cdot \boldsymbol{N} + \boldsymbol{L}(\boldsymbol{Q} \cdot \boldsymbol{N}) = \boldsymbol{t}_0^P \quad \text{on } \partial\mathcal{B}_0 \tag{10}$$

$$\boldsymbol{Q} : [\boldsymbol{N} \otimes \boldsymbol{N}] = \boldsymbol{t}_0^Q \quad \text{on } \partial\mathcal{B}_0 \tag{11}$$

where $\boldsymbol{L}(\boldsymbol{Q} \cdot \boldsymbol{N})$ denotes the following differential operator

$$-\boldsymbol{L}(\boldsymbol{Q} \cdot \boldsymbol{N}) = K\boldsymbol{Q} : [\boldsymbol{N} \otimes \boldsymbol{N}] + \nabla_X^{(T)}(\boldsymbol{Q} \cdot \boldsymbol{N}) : \boldsymbol{I} \tag{12}$$

with the total curvature $K = -\nabla_X^{(T)}\boldsymbol{N} : \boldsymbol{I}$ of the surface $\partial\mathcal{B}_0$. Herein $\nabla_X^{(N)}$ and $\nabla_X^{(T)}$ denote the normal and tangential components of the gradient. A detailed derivation of these equations is presented in the Appendix.

2.3. Piola transform of the balance of momentum

To establish the balance of linear momentum in material parameterization and spatial reference a one-sided push forward – a Piola transformation – is applied to the balance of momentum, Eq. (9), in order to rewrite them in terms of purely spatial stress tensors. For this purpose the Piola transformation formulae

$$\{\bullet\} \mapsto j\{\bullet\} \cdot \boldsymbol{F}^T \tag{13}$$

is used with $j = 1/J = dV/dv$, as the inverse Jacobian determinant. Eq. (13) relates $\mathrm{Div}(\{\bullet\}) = J\mathrm{div}(j\{\bullet\} \cdot \boldsymbol{F}^T)$, the divergence operator $\mathrm{Div}(\{\bullet\})$ with respect to material placement to the divergence operator with respect to

[2]The derivatives of values with respect to tensors of any order are denoted by $\partial_{\{\bullet\}}\{\circ\} = \frac{\partial\{\circ\}}{\partial\{\bullet\}}$. Additionally for the sake of clarity, $D_{\{\bullet\}}\{\circ\} = \frac{\partial\{\circ\}}{\partial\{\bullet\}}\Big|_X$ denotes the derivative with respect to a variable at fixed material placement $\boldsymbol{X}$.

[3]Here : denotes a double contraction of rank-two tensors $\boldsymbol{P}$ and $\boldsymbol{F}$, i.e., $P_{iJ}F_{iJ}$ and $\vdots$ denotes a triple contraction of rank-three tensors $\boldsymbol{Q}$ and $\boldsymbol{G}$, i.e., $Q_{iJK}G_{iJK}$.

[4]The divergence operators identify as: $\mathrm{Div}\,(\{\bullet\}) := \nabla_X\{\bullet\} : \boldsymbol{I}$, with respect to material coordinates $\boldsymbol{X}$.

the spatial placement div({•}). With this transformation, we obtain the (gradient enhanced) Cauchy stress and convected hyperstress[5] as

$$\boldsymbol{\sigma} := j\left[\boldsymbol{P}\cdot\boldsymbol{F}^T + \boldsymbol{Q}\overset{2,3}{\vdots}\boldsymbol{G}\right] \text{ and } \boldsymbol{\tau} = j\boldsymbol{Q} : \left[\boldsymbol{F}^T\overline{\otimes}\boldsymbol{F}^T\right] \tag{14}$$

On using the divergence relation $\mathrm{Div}\left(\boldsymbol{P} - \mathrm{Div}\boldsymbol{Q}\right) = J\,\mathrm{div}(j\left[\boldsymbol{P} - \mathrm{Div}\boldsymbol{Q}\right]\cdot\boldsymbol{F}^T)$ and also $j\left[\mathrm{Div}\boldsymbol{Q}\right]\cdot\boldsymbol{F}^T = \mathrm{div}(j\boldsymbol{Q} : \left[\boldsymbol{F}^T\overline{\otimes}\boldsymbol{F}^T\right]) - j\boldsymbol{Q}\overset{2,3}{\vdots}\boldsymbol{G}$ and $j\boldsymbol{b}_0 = \boldsymbol{b}_t$, the balance of linear momentum with material parameterization and spatial reference is given by [6]

$$\mathrm{div}(\boldsymbol{\sigma} - \mathrm{div}\,\boldsymbol{\tau}) = -\boldsymbol{b}_{\mathrm{t}}. \tag{15}$$

2.4. Constitutive assumption for stored energy density

A hyperelastic constitutive theory is chosen. The constitutive relation is appropriately chosen including a length scale parameter l. Using this constitutive assumption, various stress measures are derived for the spatial motion problem. For the internally stored energy density W_0, we assume the following hyperelastic constitutive function

$$W_0\left(\boldsymbol{F},\boldsymbol{G}\right) = \frac{1}{2}\lambda\ln^2 J + \frac{1}{2}\mu\left[\boldsymbol{F}:\boldsymbol{F} - n^{\mathrm{dim}} - 2\ln J\right] + \frac{1}{2}\mu l^2\boldsymbol{G}\vdots\boldsymbol{G}, \tag{16}$$

which consists of a Neo-Hookean term and an additional length scale term which takes into account the second-order gradients. Herein, the material parameters λ and μ are the Lamé constants from classical elasticity. Additionally, the so called internal length l, accounts for the scale dependence and may be interpreted as a characteristic size at the corresponding length. Furthermore, n^{dim} denotes the number of space dimensions. With this constitutive assumption the Piola type stresses take the form

$$\boldsymbol{P} = D_F W_0 = \left[\lambda\ln J - \mu\right]\boldsymbol{F}^{-T} + \mu\boldsymbol{F}, \tag{17a}$$

$$\boldsymbol{Q} = D_G W_0 = \mu l^2\boldsymbol{G}. \tag{17b}$$

Moreover, the Cauchy type stresses are eventually evaluated as

$$\boldsymbol{\sigma} = j\left[\left[\lambda\ln J - \mu\right]\boldsymbol{F}^{-T} + \mu\boldsymbol{F}\right]\cdot\boldsymbol{F}^T + j\mu l^2\boldsymbol{G}\overset{2,3}{\vdots}\boldsymbol{G}, \tag{18a}$$

$$\boldsymbol{\tau} = j\mu l^2\boldsymbol{G} : \left[\boldsymbol{F}^T\overline{\otimes}\boldsymbol{F}^T\right] \tag{18b}$$

3. C^1 natural neighbor interpolation

It is evident from Eq. (9) to Eq. (12) that the balance of momentum equation is of fourth order and requires an approximation which is C^1 continuous. To achieve this in the present work we pursue an implementation of gradient continua using the conformal α-natural element method (hereafter, as in Cueto *et al.* (2000), we refer to it as α-NEM). The α-NEM allows the construction of models entirely in terms of nodes, reproduces the whole domain and also ensures quadratic precision of the interpolant over convex and non-convex boundaries. A brief description of C^0 and C^1 natural neighbor interpolation schemes follows.

---

[5] $\boldsymbol{Q}\overset{2,3}{\vdots}\boldsymbol{G}$ denotes a double contraction of two rank three tensors with respect to the second and third index i.e., $Q_{aJK}G_{bJK}$

[6] The regular and modified dyadic products of two second order tensors are defined through the relations

$[\boldsymbol{A}\otimes\boldsymbol{B}] : \boldsymbol{C} = [\boldsymbol{B} : \boldsymbol{C}]\,\boldsymbol{A},\quad \boldsymbol{A} : [\boldsymbol{B}\otimes\boldsymbol{C}] = [\boldsymbol{A} : \boldsymbol{B}]\,\boldsymbol{C}$

$\left[\boldsymbol{A}\overline{\otimes}\boldsymbol{B}\right] : \boldsymbol{C} = \boldsymbol{A}\cdot\boldsymbol{C}\cdot\boldsymbol{B}^T,\quad \boldsymbol{A} : \left[\boldsymbol{B}\overline{\otimes}\boldsymbol{C}\right] = \boldsymbol{B}^T\cdot\boldsymbol{A}\cdot\boldsymbol{C}$

$\left[\boldsymbol{A}\underline{\otimes}\boldsymbol{B}\right] : \boldsymbol{C} = \boldsymbol{A}\cdot\boldsymbol{C}^T\cdot\boldsymbol{B}^T,\quad \boldsymbol{A} : \left[\boldsymbol{B}\underline{\otimes}\boldsymbol{C}\right] = \boldsymbol{B}^T\cdot\boldsymbol{A}^T\cdot\boldsymbol{C}$

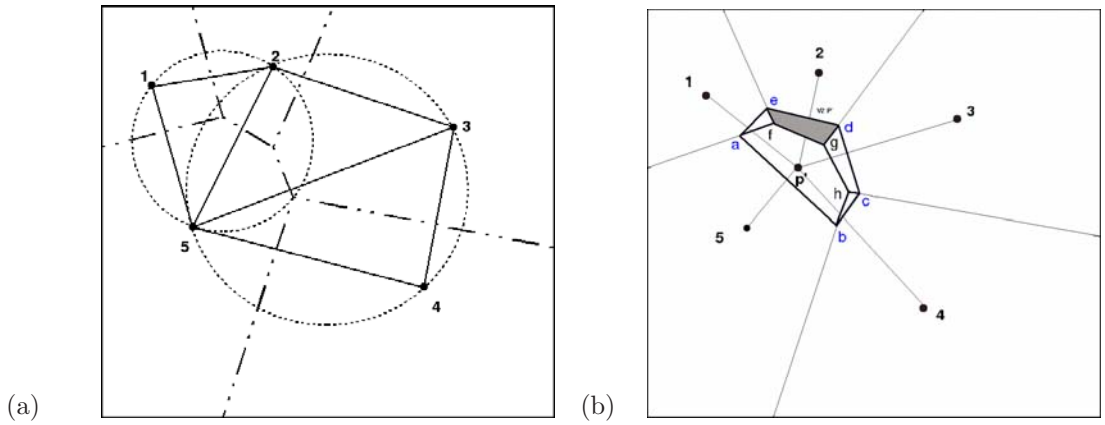

Figure 2: (a) First order Voronoi diagram and Delaunay triangulation of a set of five points; and (b) Second-order Voronoi and Sibson interpolant of p' with respect to node 2.

Consider a set of nodes $N = \{n_1, n_2, \ldots, n_M\} \in \Re^2$. Natural neighbor coordinates are constructed on the basis of the underlying Voronoi tessellation for the nodal set N. The first order Voronoi diagram of the set N is a subdivision of the plane into cells V_I (Voronoi polygons) such that any point in V_I is closer to node n_I than to any other node $n_J \in N$:

$$V_I = \left\{ \boldsymbol{X} \in \Re^2 : d(\boldsymbol{X}, \boldsymbol{X}_I) < d(\boldsymbol{X}, \boldsymbol{X}_J) \; \forall J \neq I \right\} \tag{19}$$

where $d(\cdot, \cdot)$, the Euclidean metric, is the distance between $\boldsymbol{X}_I$ and $\boldsymbol{X}_J$. The first-order Voronoi diagram, its dual the Delaunay triangulation, and the empty circumcircles for the set N are shown in Figure 2a. Now a point p' is introduced into the Voronoi diagram of set N. If p' is tessellated along with the nodal set N, then, in the newly constructed triangulation based on N and p', the natural neighbors of p' are those nodes that are connected by a Delaunay edge to p'. The C^0 natural neighbor interpolant of p' with respect to the natural neighbor node 2 is defined as the ratio of the area of overlap of the Voronoi cell, $V_{2p'}$, to the total area of the Voronoi cell of p', that is

$$\phi_2(p') = \frac{area\,(\boldsymbol{defg})}{area\,(\boldsymbol{abcde})} = \frac{A_2(p')}{A(p')}. \tag{20}$$

Thus, for any natural neighbor node I, the ratio of the area of overlap of the Voronoi cells to the total area of the Voronoi cell of p' is

$$\phi_I(p') = \frac{A_I(p')}{A(p')}, \tag{21}$$

where

$$A(p') = \sum_{I=1}^{n} A_I(p'). \tag{22}$$

To achieve C^1 natural neighbor interpolation, we adopt the procedure proposed by Sukumar and Moran (1999). The methodology is based on embedding the C^0 natural neighbor interpolant in the Bernstein-Bézier representation of a cubic simplex, termed as Farin's interpolant (see Farin (1990)) and performing a simple transformation to relate the Bézier ordinates to the nodal degrees of freedom. Let the point $p' \in \Omega \subset \Re^2$ have n natural neighbors, with $\phi_I(p')$ as the natural neighbor interpolant of node $I\,(I = 1, n)$. Let this set be defined by $\Phi = (\phi_1(p'), \phi_2(p'), \phi_3(p').....\phi_n(p'))$. These C^0 natural neighbor interpolants are identical to the barycentric

coordinates of a simplex $\delta \in \Re^{n-1}$. Following a multi-index notation[7], a Bernstein-Bézier cubic surface ($m = 3$) over the simplex δ can be written in the form

$$w^3(\Phi) = \sum_{|\mathbf{i}|=3} B^3_{\mathbf{i}}(\Phi) b_{\mathbf{i}}, \tag{23}$$

which is the C^1 interpolant used as a trial function in the natural element method. In the above equation, $B^3_{\mathbf{i}}(\Phi) = \binom{3}{\mathbf{i}} \phi_1^{i_1} \phi_2^{i_2} \ldots\ldots\ldots \phi_n^{i_n}$, where $|\mathbf{i}| = i_1 + i_2 + i_3 + \ldots + i_n = 3$. The Bézier ordinate $b_{\mathbf{i}}$ is associated with the control point $\mathbf{q_i} \in \Re^2$, where $\mathbf{q_i}$ are the projection of control points of m-variate Bézier polynomials over the $n-1$ dimensional simplex on to the plane

$$\mathbf{q_i} = \sum_{|\mathbf{j}|=1} B^1_{\mathbf{j}}(\mathbf{i}/3)\, \boldsymbol{X}_{\mathbf{j}}, \;\; |\mathbf{i}| = 3 \tag{24}$$

For more details on Bernstein-Bézier representation the reader can refer to Farin (1985). Following the procedure outlined in Sukumar and Moran (1999), now the C^1 interpolant, which is a function of Bézier ordinates, as given in Eq. (23), is transformed to a function of nodal function values and nodal gradient values by a simple transformation of the form

$$w^h(\Phi) = \{B(\Phi)\}^T \{b\} = \{B(\Phi)\}^T [T] \{w\} = \{\Psi(\Phi)\}^T \{w\}. \tag{25}$$

On constructing the transformation matrix $[T]$ (see Sukumar and Moran (1999) for more details), we can express the $C^1(\Omega)$ NEM trial function in standard shape function notation as

$$w^h(p') = \sum_{J=1}^{3n} \psi_J(p')\, d_J, \tag{26}$$

where $\psi_{3I-2}(p')$, $\psi_{3I-1}(p')$, and $\psi_{3I}(p')$ are the shape functions of node I that are associated with the d_J given by $d_J = \{d_{3I-2}, d_{3I-1}, d_{3I}\} = \{w_I, w_{I,X}, w_{I,Y}\}$, which is a function of nodal function values w_I and nodal gradient values $w_{I,X}$ and $w_{I,Y}$. The C^1 shape functions are shown in Figure 3.

Most of the properties of the $C^0(\Omega)$ natural neighbor shape functions and Bernstein-Bézier shape functions are retained by $C^1(\Omega)$ shape functions. $C^1(\Omega)$ NEM shape functions posses properties such as partition of unity, quadratic completeness, positivity and interpolation. The C^1 NEM interpolant interpolates to nodal function values and nodal gradient values, and this property makes it a suitable candidate for use in a gradient continuum formulation.

$$\begin{array}{lll} \psi_{3I-2}(\boldsymbol{X}_J) = \delta_{IJ} & \psi_{3I-1}(\boldsymbol{X}_J) = 0 & \psi_{3I}(\boldsymbol{X}_J) = 0 \\ \psi_{3I-2,X}(\boldsymbol{X}_J) = 0 & \psi_{3I-1,X}(\boldsymbol{X}_J) = \delta_{IJ} & \psi_{3I,X}(\boldsymbol{X}_J) = 0 \\ \psi_{3I-2,Y}(\boldsymbol{X}_J) = 0 & \psi_{3I-1,Y}(\boldsymbol{X}_J) = 0 & \psi_{3I,Y}(\boldsymbol{X}_J) = \delta_{IJ} \end{array} \tag{27}$$

4. C^1 natural element method for gradient continua

Equation (Eq. (9) - Eq. (12)) is a fourth order equation analogous to the biharmonic equation of Kirchoff plates. The solution to this equation thus requires C^1 continuous approximations. To this end, we use the C^1 natural neighbour approximation, both for the deformation map and for the space of admissible variations.

Now, for a gradient continuum, we write the C^1 natural neighbour approximation as a sum of deformation and gradients of deformation degrees of freedom given by

$$\boldsymbol{\varphi}^h(\boldsymbol{X}) = \sum_{a=1}^{n} \boldsymbol{\varphi}^a N^a(\boldsymbol{X}) + \sum_{a=1}^{n} \boldsymbol{F}^a \cdot \boldsymbol{M}^a(\boldsymbol{X}), \tag{28}$$

[7] Multi-indices are n-tuples of nonnegative integers, the components of which start at zero; with the norm defined as $|\mathbf{i}| = m = i_1 + i_2 + ... + i_n$.

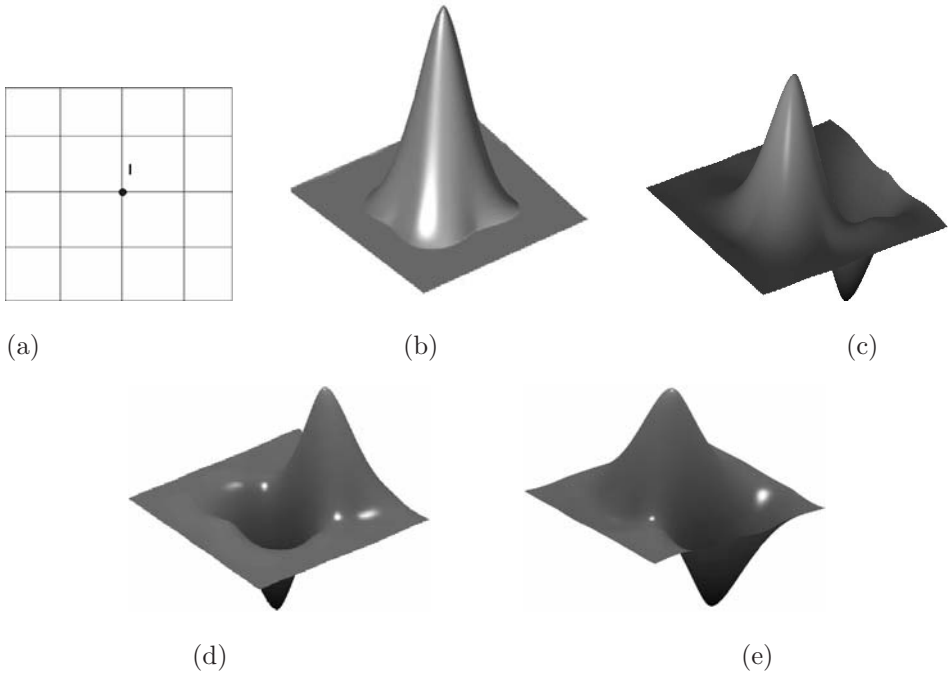

Figure 3: (a) Grid (b) C^1 Shape function ψ_{3I-2} at node I (c) Derivative $\psi_{3I-2,X}$ of C^1 shape function at node I (d) C^1 shape functions ψ_{3I-1} and (e) ψ_{3I}.

$$\delta\boldsymbol{\varphi}^h(\boldsymbol{X}) = \sum_{b=1}^{n} \delta\boldsymbol{\varphi}^b N^b(\boldsymbol{X}) + \sum_{b=1}^{n} \delta\boldsymbol{F}^b \cdot \boldsymbol{M}^b(\boldsymbol{X}), \tag{29}$$

where $N^a(\boldsymbol{X})$ and $\boldsymbol{M}^a(\boldsymbol{X})$ are the shape functions for the node a that are associated with nodal deformations $\boldsymbol{\varphi}^a$ and nodal deformation gradients $\boldsymbol{F}^a$, respectively. Herein, the nodal indices a and b account for the discrete values of the unknown $\boldsymbol{\varphi}$ and its gradients. These shape functions have the interpolating property. The first and second order deformation gradients are given by

$$\boldsymbol{F}^h = \sum_{a=1}^{n} \boldsymbol{\varphi}^a \otimes \nabla_X N^a + \boldsymbol{F}^a \cdot \nabla_X \boldsymbol{M}^a, \tag{30a}$$

$$\boldsymbol{G}^h = \sum_{a=1}^{n} \boldsymbol{\varphi}^a \otimes \nabla_X \nabla_X N^a + \boldsymbol{F}^a \cdot \nabla_X \nabla_X \boldsymbol{M}^a. \tag{30b}$$

In order to obtain the discretized spatial equilibrium equations, recall the spatial virtual work Eq. (7). Introducing the interpolation for $\delta\boldsymbol{\varphi}$ we have

$$\delta\Pi(\boldsymbol{\varphi}^h; \delta\boldsymbol{\varphi}^a, \delta\boldsymbol{F}^a) = \int_{B_0} \boldsymbol{P}(\boldsymbol{\varphi}^h) : \left[\sum_{a=1}^{n} \delta\boldsymbol{\varphi}^a \otimes \nabla_X N^a + \delta\boldsymbol{F}^a \cdot \nabla_X \boldsymbol{M}^a\right] dV \tag{31}$$

$$+ \int_{B_0} \boldsymbol{Q}(\boldsymbol{\varphi}^h) \vdots \left[\sum_{a=1}^{n} \delta\boldsymbol{\varphi}^a \otimes \nabla_X \nabla_X N^a + \delta\boldsymbol{F}^a \cdot \nabla_X \nabla_X \boldsymbol{M}^a\right] dV + \delta\Pi^{ext}(\boldsymbol{\varphi}^h),$$

The above equation can be rearranged for all $\delta\boldsymbol{\varphi}^a$ and $\delta\boldsymbol{F}^a$ as

$$\delta\Pi(\boldsymbol{\varphi}^h;\delta\boldsymbol{\varphi}^a,\delta\boldsymbol{F}^a)=\sum_{a=1}^{n}\delta\boldsymbol{\varphi}^a\cdot\int\limits_{\mathcal{B}_0}\left[\boldsymbol{P}(\boldsymbol{\varphi}^h)\cdot\nabla_X N^a+\boldsymbol{Q}(\boldsymbol{\varphi}^h):\nabla_X\nabla_X N^a\right]dV \tag{32}$$

$$+\sum_{a=1}^{n}\delta\boldsymbol{F}^a:\int\limits_{\mathcal{B}_0}\left[\boldsymbol{P}(\boldsymbol{\varphi}^h)\overset{2}{\cdot}\nabla_X\boldsymbol{M}^a+\boldsymbol{Q}(\boldsymbol{\varphi}^h)\overset{2,3}{\vdots}\nabla_X\nabla_X\boldsymbol{M}^a\right]dV+\delta\Pi^{ext}(\boldsymbol{\varphi}^h)=0.$$

The discrete residuals[8] of the spatial motion problem can thus be written as

$$\boldsymbol{R}_a^{\varphi}=\int\limits_{\mathcal{B}_0}\boldsymbol{P}(\boldsymbol{\varphi}^h)\cdot\nabla_X N^a(\boldsymbol{X})dV+\int\limits_{\mathcal{B}_0}\boldsymbol{Q}\left(\boldsymbol{\varphi}^h\right):\nabla_X\nabla_X N^a\left(\boldsymbol{X}\right)dV-\boldsymbol{F}_a^{\varphi^{ext}}=\boldsymbol{0}. \tag{33a}$$

$$\boldsymbol{R}_a^{F}=\int\limits_{\mathcal{B}_0}\boldsymbol{P}(\boldsymbol{\varphi}^h)\overset{2}{\cdot}\nabla_X\boldsymbol{M}^a(\boldsymbol{X})dV+\int\limits_{\mathcal{B}_0}\boldsymbol{Q}(\boldsymbol{\varphi}^h)\overset{2,3}{\vdots}\nabla_X\nabla_X\boldsymbol{M}^a(\boldsymbol{X})dV-\boldsymbol{F}_a^{F^{ext}}=\boldsymbol{0}. \tag{33b}$$

This represents a set of nonlinear equilibrium equations with the current nodal deformation and its gradient as unknowns. The solution of these equations is achieved using a Newton Raphson iterative procedure. The linearized coupled problem

$$\begin{bmatrix}\boldsymbol{K}_{ab}^{\varphi\varphi} & \boldsymbol{K}_{ab}^{\varphi F}\\ \boldsymbol{K}_{ab}^{F\varphi} & \boldsymbol{K}_{ab}^{FF}\end{bmatrix}\begin{bmatrix}\Delta\boldsymbol{\varphi}_b\\ \Delta\boldsymbol{F}_b\end{bmatrix}=\begin{bmatrix}\boldsymbol{F}_a^{\varphi^{ext}}-\boldsymbol{F}_a^{\varphi^{int}}\\ \boldsymbol{F}_a^{F^{ext}}-\boldsymbol{F}_a^{F^{int}}\end{bmatrix}$$

is solved for increments of $\boldsymbol{\varphi}^b$ and $\boldsymbol{F}^b$. The component matrices of the global tangent stiffness matrix are given by

$$\boldsymbol{K}_{ab}^{\varphi\varphi}=\frac{\partial\boldsymbol{R}_a^{\varphi}}{\partial\boldsymbol{\varphi}_b}=\int\limits_{\mathcal{B}_0}\left[\left[D_F\boldsymbol{P}\cdot\nabla_X N^a\right]\cdot\nabla_X N^b+\left[D_G\boldsymbol{Q}:\nabla_X\nabla_X N^a\right]:\nabla_X\nabla_X N^b\right]dV \tag{34a}$$

$$\boldsymbol{K}_{ab}^{\varphi F}=\frac{\partial\boldsymbol{R}_a^{\varphi}}{\partial\boldsymbol{F}_b}=\int\limits_{\mathcal{B}_0}\left[\left[D_F\boldsymbol{P}\cdot\nabla_X N^a\right]\overset{2}{\cdot}\nabla_X\boldsymbol{M}^b+\left[D_G\boldsymbol{Q}:\nabla_X\nabla_X N^a\right]\overset{2,3}{\vdots}\nabla_X\nabla_X\boldsymbol{M}^b\right]dV \tag{34b}$$

$$\boldsymbol{K}_{ab}^{F\varphi}=\frac{\partial\boldsymbol{R}_a^{F}}{\partial\boldsymbol{\varphi}_b}=\int\limits_{\mathcal{B}_0}\left[\left[D_F\boldsymbol{P}\cdot\nabla_X\boldsymbol{M}^a\right]\overset{2}{\cdot}\nabla_X N^b+\left[D_G\boldsymbol{Q}:\nabla_X\nabla_X\boldsymbol{M}^a\right]\overset{2,3}{\vdots}\nabla_X\nabla_X N^b\right]dV \tag{34c}$$

$$\boldsymbol{K}_{ab}^{FF}=\frac{\partial\boldsymbol{R}_a^{F}}{\partial\boldsymbol{F}_b}=\int\limits_{\mathcal{B}_0}\left[\left[D_F\boldsymbol{P}\cdot\nabla_X\boldsymbol{M}^a\right]\overset{2}{\cdot}\nabla_X\boldsymbol{M}^b+\left[D_G\boldsymbol{Q}:\nabla_X\nabla_X\boldsymbol{M}^a\right]\overset{2,3}{\vdots}\nabla_X\nabla_X\boldsymbol{M}^b\right]dV \tag{34d}$$

where the specific tangent operators for the constitutive law read as

$$D_F\boldsymbol{P}=\lambda\boldsymbol{F}^{-T}\otimes\boldsymbol{F}^{-T}-\left[\lambda\ln J-\mu\right]\boldsymbol{F}^{-T}\underline{\otimes}\boldsymbol{F}^{-T}+\left[\mu\right]\boldsymbol{I}\overline{\otimes}\boldsymbol{I} \tag{35a}$$

$$D_G\boldsymbol{Q}=\mu l^2\boldsymbol{I}\underline{\otimes}\left[\boldsymbol{I}\overline{\otimes}\boldsymbol{I}\right], \tag{35b}$$

where $D_F\boldsymbol{P}$ and $D_G\boldsymbol{Q}$ are tensors of fourth and sixth order respectively. $\boldsymbol{K}_{ab}^{\varphi\varphi}$,$\boldsymbol{K}_{ab}^{\varphi F}$ and its symmetric counterpart $\boldsymbol{K}_{ab}^{F\varphi}$ and $\boldsymbol{K}_{ab}^{FF}$ are tensors of second, third, and fourth order respectively and are arranged in appropriate global locations to yield the global stiffness matrix. The symmetric bilinear form of basis functions together with continous function of nodal function values and nodal gradient values in the neighbourhood of any given evaluation point result in symmetric hessian matrix. A background cell grid with standard Gauss quadrature rule is used for numerical evaluation of these integrals.

[8] $\boldsymbol{A}\overset{2}{\cdot}\boldsymbol{B}$ denotes a contraction of rank two tensors with respect to the second index i.e., $A_{aJ}B_{bJ}$

5. On the α-shape extension to NEM

So called α-shapes define a family of simplicial complexes parameterized by $\alpha \in \mathbb{R}$. This concept was introduced by Edelsbrunner *et al.* (1983), for the study of points in the plane and higher dimensions by Edelsbrunner and Mucke (1994). Recently, density scaled α-shapes have been used in natural neighbor interpolation for imposing essential boundary conditions on non-convex domains (Cueto *et al.*, 2000). For non-uniform nodal discretization, there is a need for α shape filtration on a local scale, unlike a global scale for reconstructing the whole domain. This requires a judicious choice of α values. Conformal alpha shapes (originally proposed by Cazals *et al.* (2006)) are a potential solution for such discretizations. Let us consider a nodal point set $S \subset \mathbb{R}^d$. For a given value of $\alpha \in [0, \infty)$, $\alpha - balls$ are circles of radius α around the nodal points in S. The step by step procedure for construction of conformal α-shapes is briefly outlined here.

- For the given point set S, the Delaunay triangulation $DT(S)$ is first constructed. Figure 4a shows the Delaunay triangulation for a set consisting of 10 nodes.

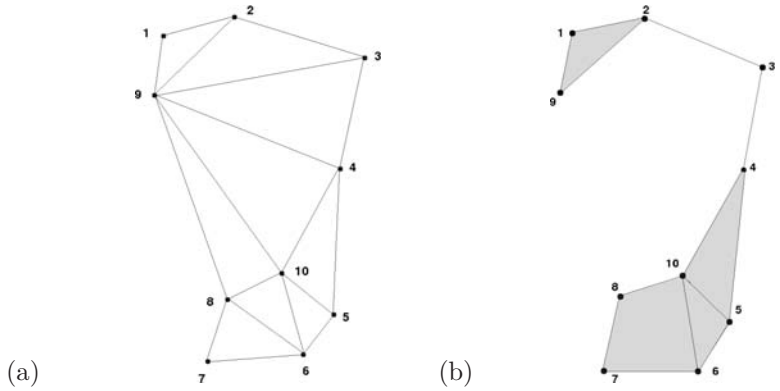

Figure 4: (a) Delaunay triangulation $DT(S)$ (b) α-complex C_α of S_α

- The boundary of the α-shape ∂S_α is part of the Delaunay triangulation $DT(S)$. Figure 5 shows the boundary ∂S_α as a collection of k-simplices[9] which are α-exposed[10]. To achieve this a list of all k-simplices, KS is computed in this step.

- Figure 6 shows boundary of α-shape as a collection of simplices. It is seen that for a range of alpha values there is a topological change in the boundary. Such simplices are termed as *critical* α-shapes. In this step, a list B_T of limits $[\alpha_i, \infty]$ of intervals such that a k-simplex belongs to the boundary ∂S_α of the critical α-shape is obtained.

- For the point set S, using KS, the α-complex[11], denoted as C_α is now constructed. For any assumed value of the radius of the great circle of a k-simplex σ_{KS} and corresponding center μ_{KS}, it is determined if a particular simplex belongs to C_α, by inspecting all simplices in $DT(S)$. To do this we check if $\sigma_{KS} < \alpha$ and the σ_{KS} ball centered at μ_{KS} is empty[12].

[9] k-simplex is a k-dimensional analouge of triangle. Specifically, a simplex is the convex hull of a set of $n+1$ affinely independent points, in some Euclidean space of dimension n or higher

[10] A k-simplex is said to be α -exposed at any point e, if there exists an empty α ball with $e \cap S = 0$ and $T = \partial e \cap S$, where ∂e is the circle bounding e

[11] The α-complex of S is the Delaunay triangulation of S, $DT(S)$ restricted to $\alpha-$ circles of radius α

[12] In constructing the α complex C_α, for any k-simplex in KS the condition of $\sigma_{KS} < \alpha$ and the σ_{KS} ball centered at μ_{KS} being empty is referred to as α test

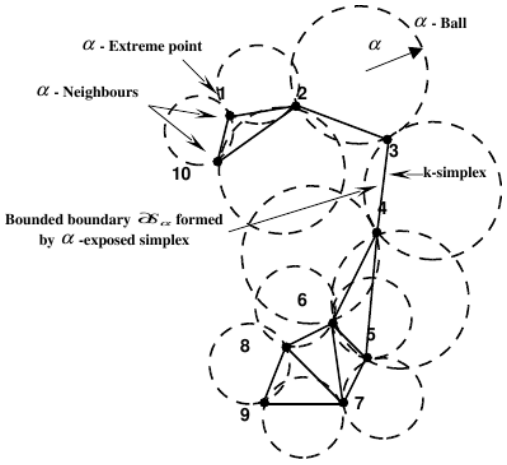

Figure 5: Boundary ∂S_α defining the evolution of α-complex.

Figure 6: Set of critical $\{\alpha_n^i\}$ simplices for range of alpha values.

- Now we get a list of all k-simplices of C_α to make up the interior of S_α and all simplices on the boundary ∂C_α form ∂S_α. Figure 5 shows the α complex C_α for the set of 10 nodes.

- Figure 7a shows a weighted distribution of point set and corresponding α-complex. For sufficiently large values of α, the α-complex is the Delaunay triangulation $DT(S)$ of S. For lower values of α, distinct features of the domain are captured as patches (see Figure 7b-d).

- When the initial distribution of points is unstructured and coarsely distributed, the construction is involved. For instance, let us consider the domain of a membrane with a hole (see Figure 8a). For larger values of α, the local features (like the hole region) remain uncaptured (see Figure 8b) , while at smaller values (see Figures 8c–8e) not all boundaries of the domain are reconstructed. It is important that the shape reconstruction procedure is able to recover all the boundaries of the domain in solid mechanics applications. To achieve this, the above steps of computing the α-complex is slightly modified in the next step.

- To reconstruct the whole boundary, we rescale the radius of the α-circle. For any point or node $n \in S$, let $DT(n) \subseteq DT(S)$ denote the simplices incident on n. The conformal α value determines a partial ordering on $DT(n)$, with $DT(n)$ considered as a sequence of simplices with non decreasing alpha values $\alpha_n^1 \leq \ldots \leq \alpha_n^n$ (see Figure 5). Now, $\alpha_n^1 = 0$, since the first simplex in $DT(n)$ is the point n which appears at $\alpha = 0$. Let $\alpha_n^- < \alpha_n^+$ be two α values in $\{\alpha_n^i\}_i$. Now, the local value of α_n^i at every point is rescaled according to

$$\hat{\alpha}_n^i = \frac{\alpha_n^i - \alpha_n^-}{\alpha_n^+}, \tag{36}$$

where $\hat{\alpha}_n^i$ is the internal α-scale. This is invariant to Euclidean transformation, and hence is termed as *conformal*. A new set of circles whose radii are dependent on internal alpha scales given by $\alpha_n(\hat{\alpha}) =$

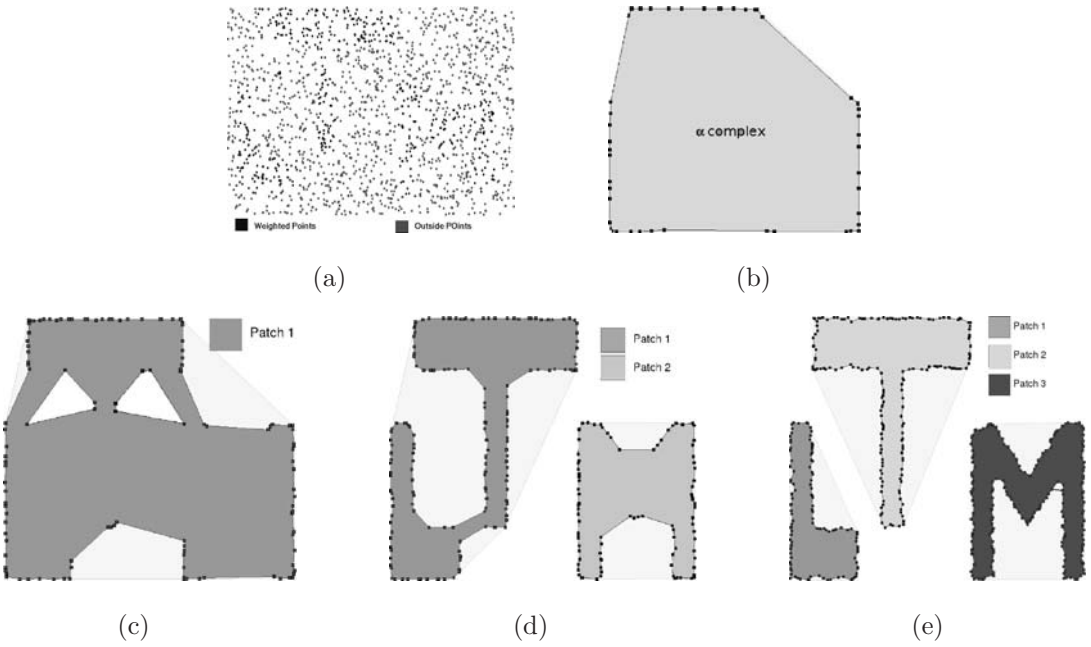

Figure 7: Evolution of critical α-complexes. (a) Weighted point set distribution; (b) $\alpha = 2$; (c) $\alpha = 0.35$; (d) $\alpha = 0.12$; and (e) $\alpha = 0.035$

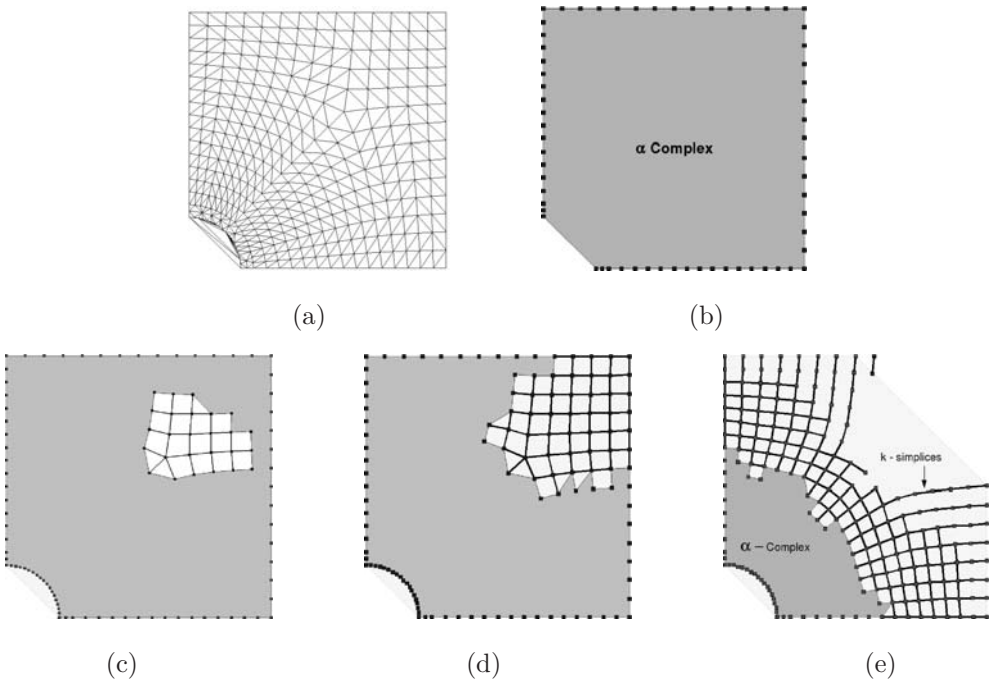

Figure 8: Evolution of critical α-complexes for a membrane with a hole. (a) Delaunay triangulation; (b) $\alpha = 1$; (c) $\alpha = 0.12$; (d) $\alpha = 0.1$; and (e) $\alpha = 0.07$.

$\alpha_n^+\hat{\alpha} + \alpha_n^-$ is considered. The *conformal α-shape complex is thus obtained by Delaunay triangulation of S, restricted to* $C_{\hat{\alpha}}$.

- The conformal shape is now constructed from the α-complex by computing the *medial axis*[13] and the *local feature size*[14]. The sampling of points is adapted according to these two values multiplied by a parameter ϵ.

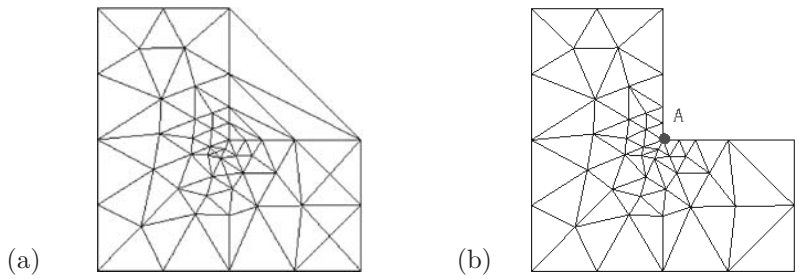

Figure 9: L-shaped domain (a) before α-shaping (b) after α-shaping

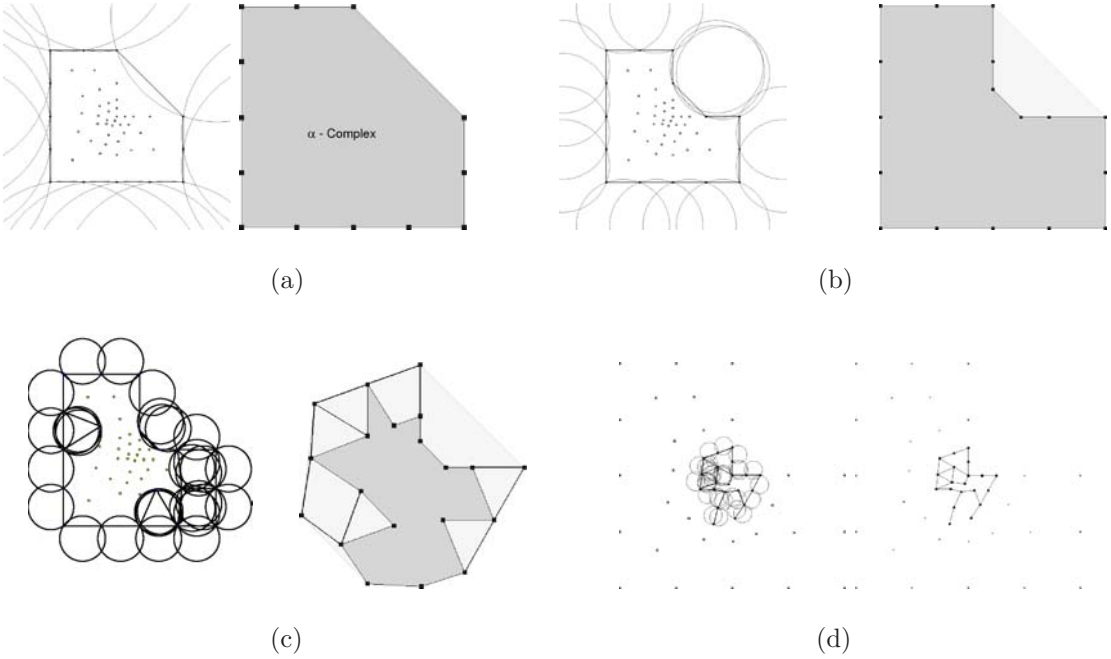

Figure 10: L-shaped domain: Critical α-simplices for (a) $\alpha = 80$ (b) $\alpha = 35$ (c) $\alpha = 15$ (d) $\alpha = 4$

[13]The medial axis $M(S)$ of any point set S is defined as the union of the centers of all maximal open balls

[14]The local feature size of any point is governed by the distance $f_r(X) = \inf_{Y \in M(S)} \|X - Y\|$) to medial axis and the corresponding implicit direction $f_\theta(X) = cos^{-1}\left(\frac{X \cdot Y}{\|X\|\|Y\|}\right)$

(a) 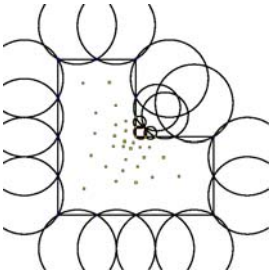 (b) 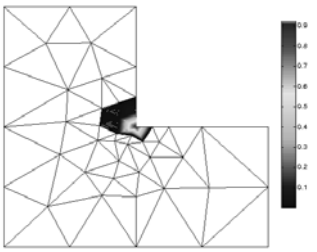

Figure 11: L-shaped domain (a) Conformal α shape; and (b) Plot of shape function at node A.

To demonstrate this, we consider an L shaped domain with irregular nodal distribution, the critical α simplices are shown in Figure 10. The conformal alpha shape for the L-shaped domain (see Figure 10a) and the plot of shape functions at the renterant corner node A is shown in Figure 10b. For a general cellular domain, the Delaunay triangulation before and after α shaping are shown in Figure 10d.

(a) 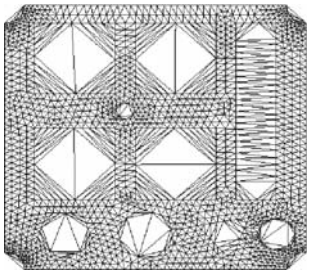 (b) 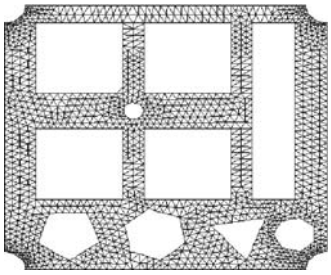

Figure 12: Cellular domain; (a) before α-shaping; and (b) after α-shaping.

6. Numerical examples

The proposed algorithm for the gradient continuum is now applied to numerical examples. Firstly, we study the convergence of numerical results by α-NEM in a geometrically non-linear setting. For this study, we consider the Cook's membrane example. Secondly, it is desired to demonstrate that the gradient elasticity theory can remove strain singularity and stress amplifications from typical examples of classical elasticity. This is shown by considering the effect of the length scale parameter in the constitutive law. We first consider a rectangular specimen with an inhomogeneity in the form of a central hole under uniaxial tension. The next examples include an L-shaped specimen subjected to shear deformation, a block under uniaxial compression and finally a rectangular specimen with an edge crack under uniform axial tension. In all these examples, the boundary conditions consists of homogeneous Neumann boundary conditions for the gradient deformation map.

6.1. Cook's membrane problem

A tapered panel clamped on one side with a shear loading on the opposite side is considered as shown in Figure 13. Lamé constants of $\lambda = 73.5$ GPa, $\mu = 36.5$ GPa and Poisson ratio $\nu = 0.25$ are considered. For the convergence study four different discretizations of 235, 722, 2767 and 6677 nodes are considered. $3 \times 3, 6 \times 6$ and 25×25 quadrature rule is used for the numerical integration in each of these cases. Uniform traction is applied in incremental steps. The displacements at node A (with coordinates $X = 48$ mm and $Y = 50.4$ mm)

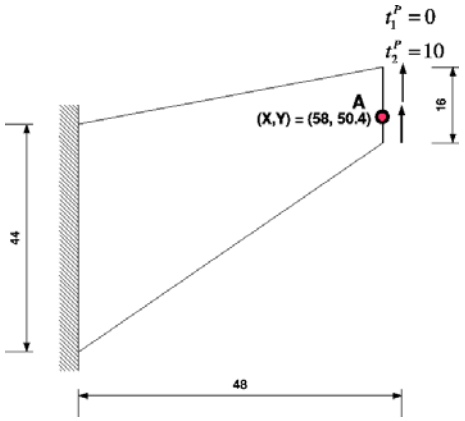

Figure 13: Cook's membrane problem

are evaluated at various load steps. Figure 14 shows the plot of the displacement computed at node A for four discretization and various quadrature rules.

It is observed that the displacement convergence has a lower bound trend, with a progressive decrease in displacements with increasing quadrature and nodal degrees of freedom. The method shows good convergence at finite strains. In a gradient continuum context, to study the effect of length scale on displacements at various load steps, the displacements were evaluated at the node A for various load steps. Five length scales of $L_0/5, L_0/10, L_0/20, L_0/40$ and L_0/∞ , where $L_0 = 48mm$ was considered. A quadrature of 25×25 was considered for the analysis. The plot of displacement with load factor (defined as the ratio of applied load at the end of a load step to maximum load) is shown in Figure 15. It is observed that the overall behavior of the specimen becomes stiffer with increasing internal length. It is very clear that the length scales has a significant and consistent effect on the displacements.

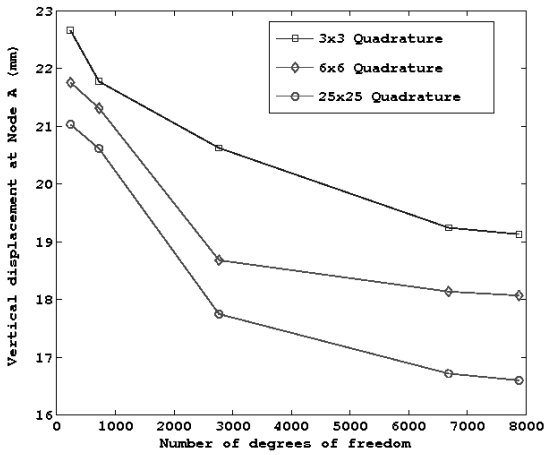

Figure 14: Plot of displacement at node A for Cook's membrane problem.

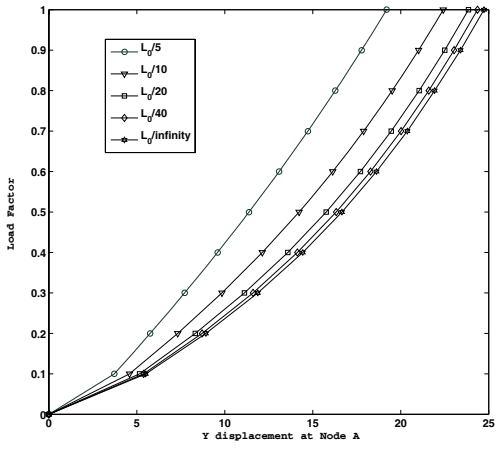

Figure 15: Plot of displacement at node A versus load factor for various length scales.

6.2. Uniaxial loading of a rectangular specimen with a hole

In a rectangular specimen of length $L_0 = 36$ and width $L_0/3$, an inhomogeneity is introduced by means of a centered circular hole of radius $r = L_0/12$, as shown in Figure 16a. The Delaunay triangulation of the grid results in triangles in the hole region. As mentioned before, it is desired to modify the neighborhood in the non-convex hole region and remove the triangles outside the domain. Thus, α-shaping is performed to reproduce the entire rectangular specimen with hole region and the final grid is as shown in Figure 16b.

The nodes at the bottom edge of the discretized geometry are fixed in longitudinal direction, a constant displacement boundary condition in the same direction is applied on the top nodes step wise, until the final length of $1.5L_0$ is reached. Lamé constants of $\lambda = 73.5$ GPa, $\mu = 36.5$ GPa and Poisson ratio of $\nu = 0.25$ are considered. Five internal length scales namely $L_0/3$, $L_0/12$, $L_0/48$, $L_0/120$ and L_0/∞ are used to investigate the effect of length scales on the stiffness and the resulting field of the Cauchy type stresses and invariants.

The residual force at the bottom is measured for various load steps. A plot of the total residual force along CD versus the displacement at top AB is plotted for various length scales as shown in Figure 17. For the same displacement there is an increase in residual force with increase in length scale. This clearly indicates that the overall behavior of the specimen become stiffer with increasing internal length.

The distribution of the Cauchy type stress component σ_{11} at various length scales is shown in Figure 18. It can be observed that the deformation of the hole is less distinct compared to the overall deformation indicating a stiffening effect with increase in length scale. Moreover the stress field is influenced more distinctively in a wider region by the inhomogeneity represented by the hole. At length scale of $l = L_0/\infty$ theoretically the results obtained from the C^1 NEM in a limiting sense are identical to those obtained from the C^0 NEM results. To study this effect, a comparison of the result is made with those obtained from the C^0 NEM and all values are plotted to the same scale as those obtained from C^0 NEM. It is seen from Figure 18 that there is a slight disturbance in the distribution of the stresses and reduction in maximum values because of possible stiffening effect with C^1 NEM when $l = L_0/\infty$. This may be attributed to the decoupling of the residuals arising from the displacements and its gradients.

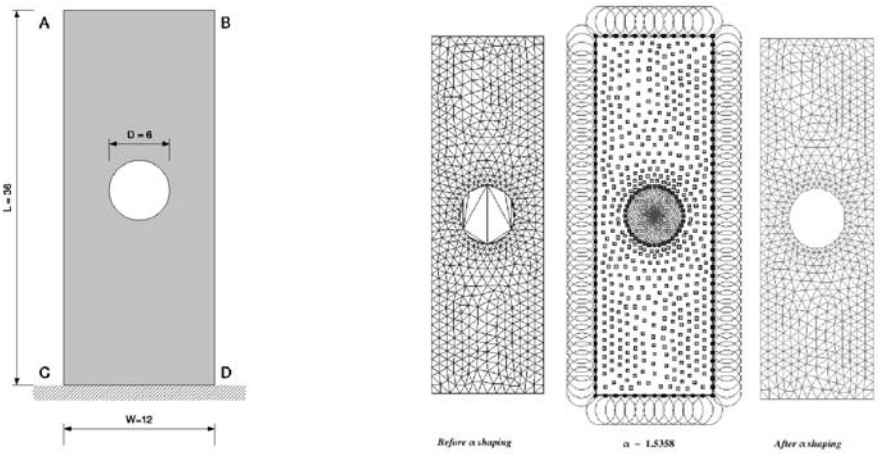

(a) (b)

Figure 16: (a) Rectangular specimen with a circular hole (b) Delaunay triangulation and discretization after α-shaping for the rectangular specimen with circular hole.

Figure 19 shows the distribution of the Cauchy type stress component σ_{22} for various length scales. Figure 20 shows a plot of the components of gradients of $\boldsymbol{F}$ at a length scale of $l = L_0/3$. It is observed that $\boldsymbol{F}$ is not symmetric. To study the effect of the Cauchy-type hyperstress with length scale a double stress invariant I_Q defined as $I_Q := \tau^2_{111} + \tau^2_{222} + \tau^2_{122} + \tau^2_{211}$ is computed. Figure 21 shows the plot of the double stress invariant

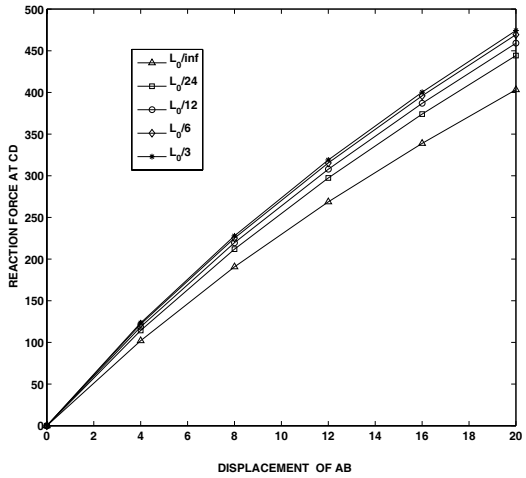

Figure 17: Plot of displacements along AB versus reaction force at CD for various length scales for the rectangular specimen with a circular hole.

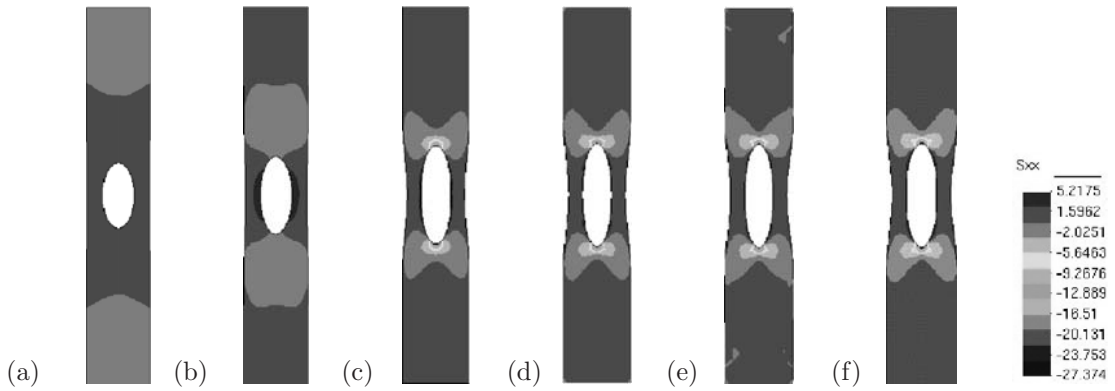

Figure 18: Plot of Cauchy type stresses σ_{11} at various length scales for rectangular specimen with circular hole (a) $l = L_0/3$ (b) $l = L_0/12$ (c) $l = L_0/48$ (d) $l = L_0/120$ (e) $l = L_0/\infty$ (f) L_0/∞ C^0-NEM

for various length scales. At larger length scales the effect of double stress is dominant, and results in increased stiffness.

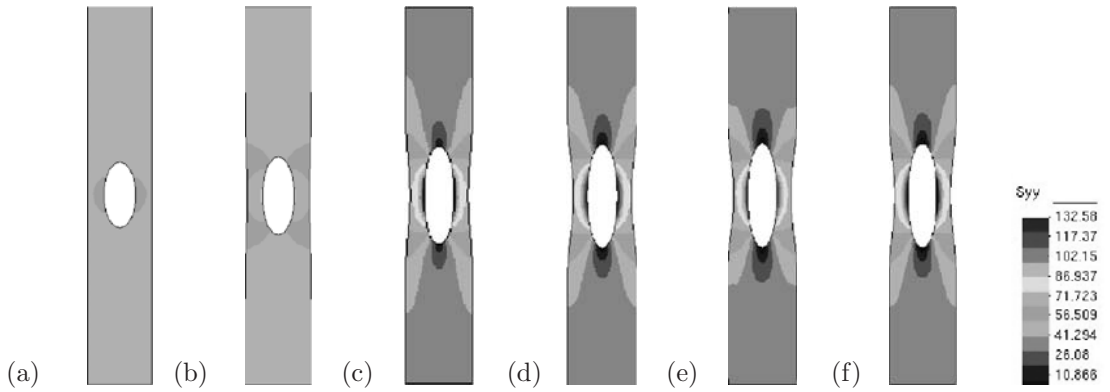

Figure 19: Plot of Cauchy type stresses σ_{22} at various length scales for rectangular specimen with circular hole (a) $l = L_0/3$ (b) $l = L_0/12$ (c) $l = L_0/48$ (d) $l = L_0/120$ (e) $l = L_0/\infty$ (f) $L_0/\infty\, C^0$-NEM .

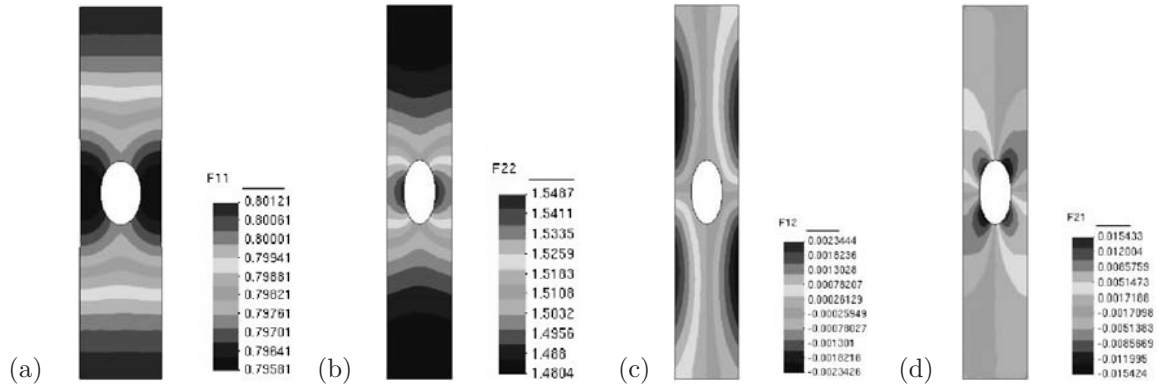

Figure 20: Plot of deformation gradient degrees of freedom (a) $\boldsymbol{F}_{11}$(b)$\boldsymbol{F}_{22}$ (c) $\boldsymbol{F}_{12}$ (d) $\boldsymbol{F}_{21}$ at length scale of $l = L_0/3$ for rectangular specimen with circular hole.

6.3. Biaxial loading of a L-shaped specimen

A L-shaped specimen of the dimensions shown in Figure 22 is considered. The initial discretization is shown in Figure 23. To reproduce the shape along non-convex boundaries a conformal α-shaping as discussed in the previous section has been performed. The specimen is subjected to a prescribed displacement in the X direction along EF and Y direction along BC.

To prevent rigid body motion all the deformation degrees of freedom at the re-entrant corner are additionally fixed. The Lamé constants are taken as $\lambda = 73.5$ GPa, $\mu = 36.5$ GPa and Poisson ratio $\nu = 0.25$ for the analysis. The analysis is performed for five length scales, namely $L_0/2$, $L_0/5$, $L_0/10$, $L_0/100$ and L_0/∞. The plot of the Cauchy type stress σ_{11}, σ_{22} and σ_{12} for various length scales are shown in Figure 24, Figure 25 and Figure 26, respectively. From these plots it is again observed that increasing the length scale makes the system stiffer and the stress distribution is spread out and is less affected by the re-entrant corner. A plot of the variation of the double stress invariant I_Q for various length scales is shown in Figure 27.

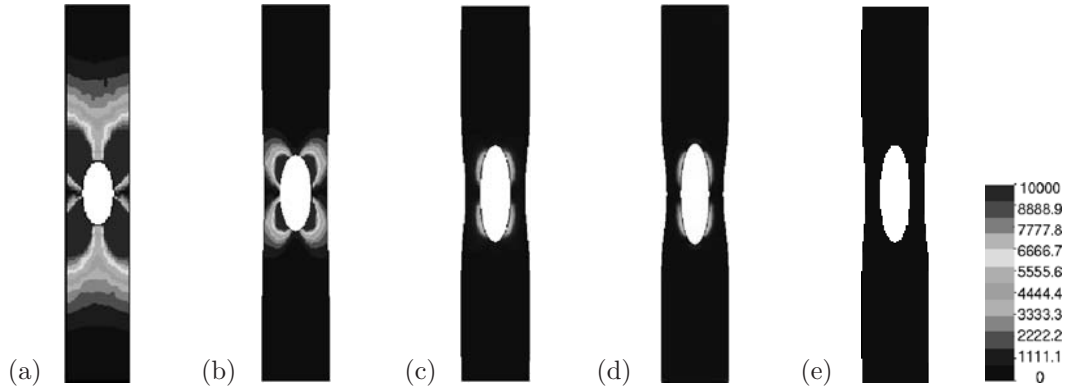

Figure 21: Plot of double stress invariant I_Q at various length scales for rectangular specimen with circular hole.(a) $l = L_0/3$ (b) $l = L_0/12$ (c) $l = L_0/48$ (d) $l = L_0/120$ (e) $l = L_0/\infty$

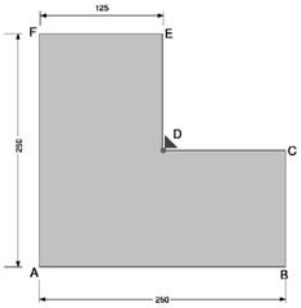

Figure 22: L-shaped specimen under biaxial loading.

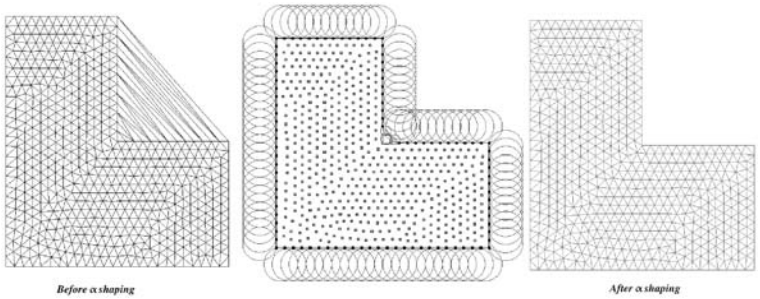

Figure 23: Discretization of L-shaped example.

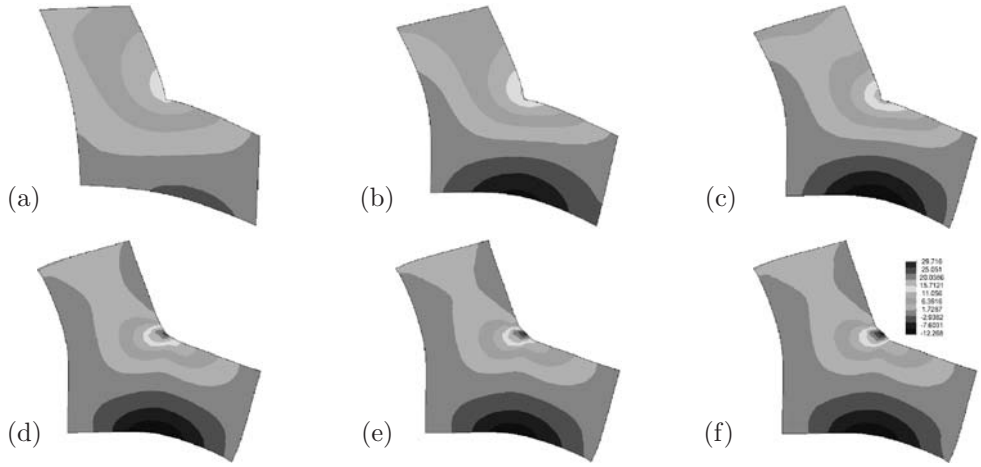

Figure 24: Plot of Cauchy stress σ_{11} at various length scales for L-shaped example.(a) $l = L_0/2$ (b) $l = L_0/5$ (c) $l = L_0/10$ (d) $l = L_0/100$ (e) $l = L_0/\infty$ (f) $l = L_0/\infty$ C^0 NEM

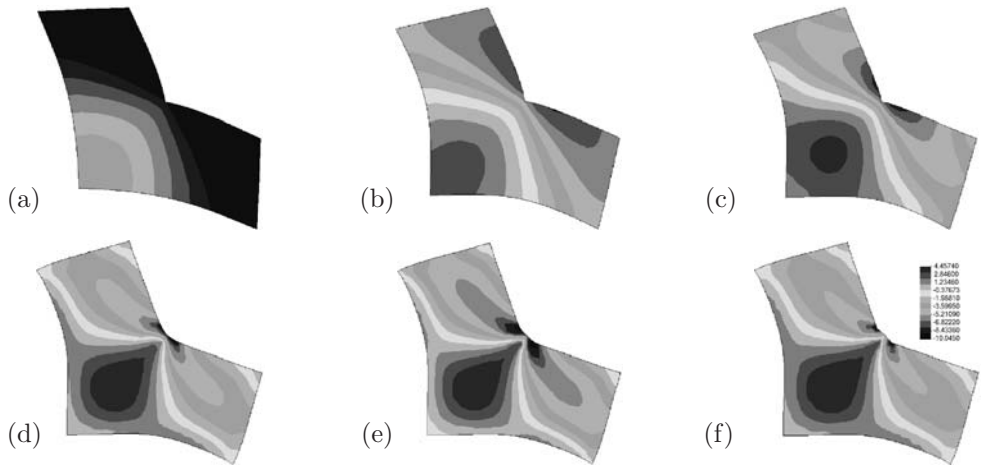

Figure 25: Plot of Cauchy stress $\sigma_{12} = \sigma_{21}$ at various length scales for L-shaped example.(a) $l = L_0/2$ (b) $l = L_0/5$ (c)$l = L_0/10$ (d) $l = L_0/100$ (e) $l = L_0/\infty$ (f) $l = L_0/\infty\, C^0$ -NEM

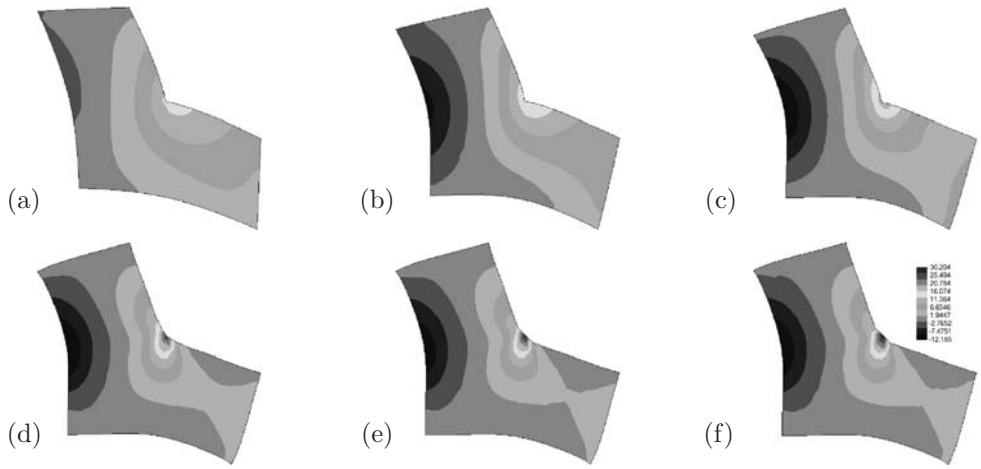

Figure 26: Plot of Cauchy stress σ_{22} at various length scales for L-shaped example.(a) $l = L_0/2$ (b) $l = L_0/5$ (c)$l = L_0/10$ (d) $l = L_0/100$ (e) $l = L_0/\infty$ (f) $l = L_0/\infty\, C^0$ -NEM

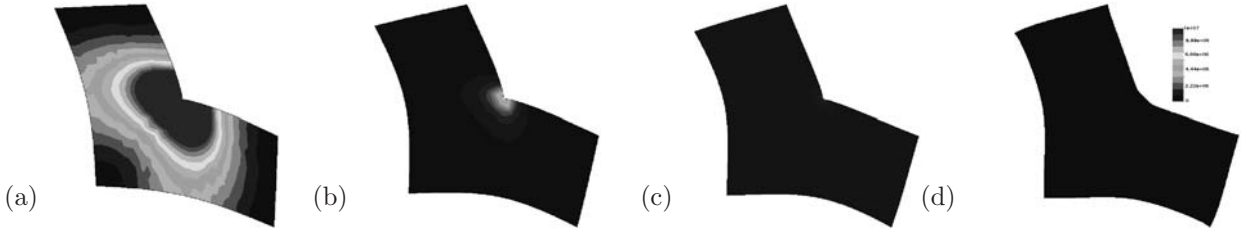

Figure 27: Plot of double stress invariant I_Q at various length scales for L-shaped example.(a) $l = L_0/2$ (b) $l = L_0/5$ (c)$l = L_0/10$ (d) $l = L_0/\infty$

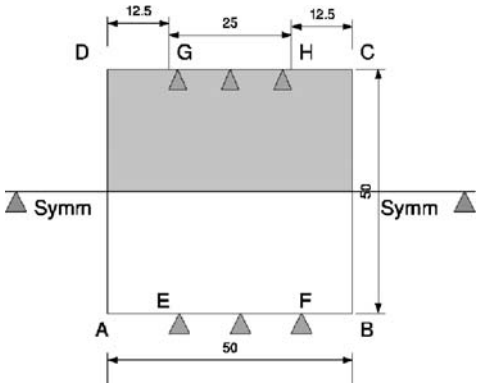

Figure 28: Square block example.

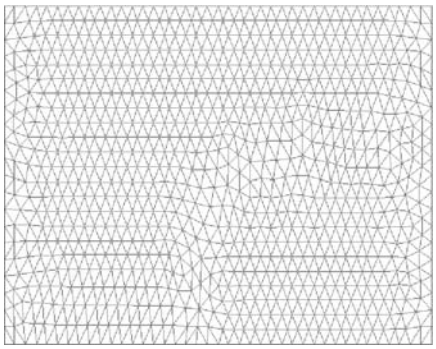

Figure 29: Discretization for the square block example.

6.4. Uniaxial compression of a square block

A square block of the dimensions shown in Figure 28 is subjected to a non-uniform compression. Displacements are applied along EF and GH so as to induce non uniform compression. It is desired to investigate the resulting Cauchy stress distribution at various length scales. Because of the symmetry only one-half of the block is considered for convenience. The block is discretized as shown in Figure 29. Figure 30 shows the distribution of the Cauchy stress σ_{11} at various length scales. Figure 31 and Figure 32 display the distribution of the Cauchy stress σ_{22} and σ_{12} at various length scales. Again the main feature to observe is that the overall behavior of the specimen becomes stiffer with increasing internal length.

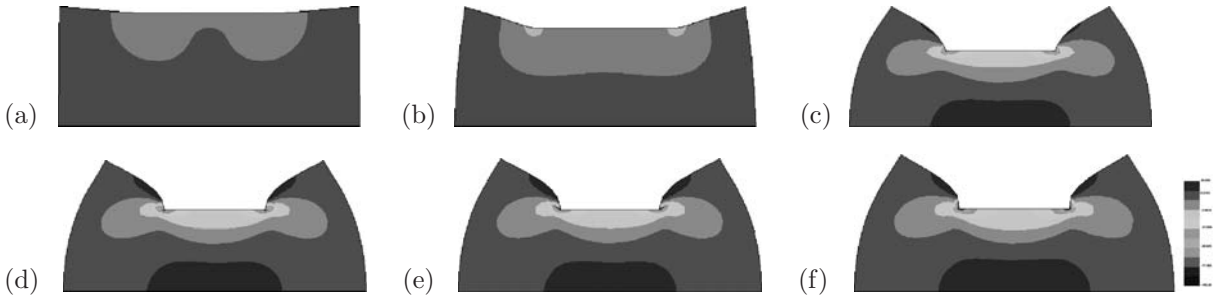

Figure 30: Plot of Cauchy stress σ_{11} at various length scales for the square block example. (a) $l = L_0/2$ (b) $l = L_0/5$ (c) $l = L_0/10$ (d) $l = L_0/100$ (e) $l = L_0/\infty$ (f) $l = L_0/\infty$ (g) C^0-NEM

6.5. Uniaxial loading of a cracked specimen

A rectangular specimen with an edge crack under uniaxial quasi-static loading is considered (see Figure 33a). The discretization is shown in Figure 33b. The displacements at the bottom edge AB is fixed and uniaxial displacement is applied at the top edge CD. The neighborhood at the crack edge is modified by imposing a visibility criterion as given in Sukumar *et al.* (1998). The influence of the variation of length scale on the Cauchy type stresses are studied. Five length scales $L_0/4$, $L_0/10$, $L_0/50$, $L_0/100$ and L_0/∞ are considered for the analysis. For the variation of the internal length the Cauchy type stress σ_{11} is plotted in Figure 34. Figure 35 shows the distribution of the normal component of the Cauchy stress σ_{22} in the loading direction. A comparison of the stresses at zero length scale is made with those obtained from C^0 NEM. It is observed that the possible decoupling between the residuals results in a slight disturbance of stresses obtained from C^1 NEM. The double stress invariants are shown in Figure 36. The plot indicates the increase in the stiffness with length scales.

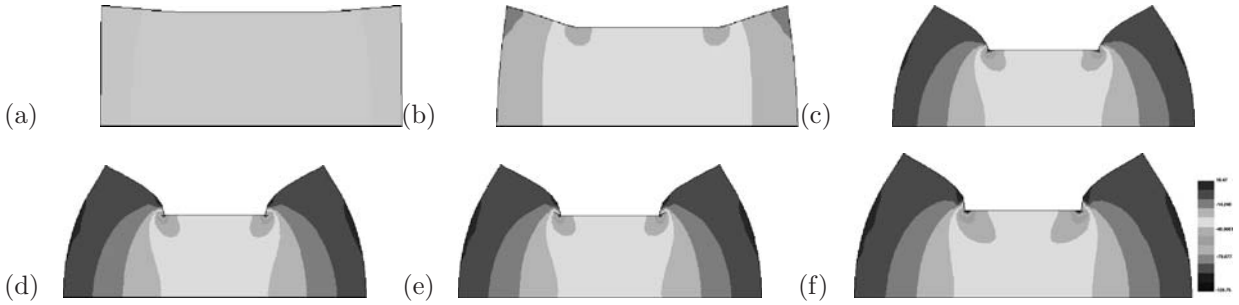

Figure 31: Plot of Cauchy stress σ_{22} at various length scales for the square block example. (a) $l = L_0/2$ (b) $l = L_0/5$ (c) $l = L_0/10$ (d) $l = L_0/100$ (e) $l = L_0/\infty$ (f) $l = L_0/\infty$ (g) C^0-NEM

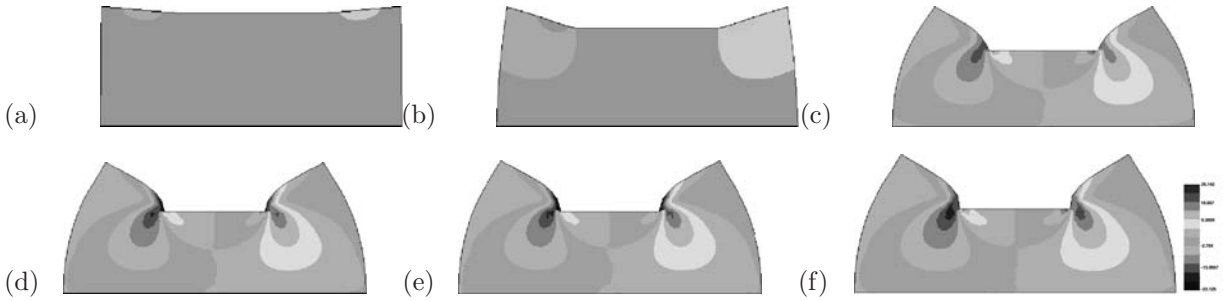

Figure 32: Plot of Cauchy stress $\sigma_{12} = \sigma_{21}$ at various length scales for the square block example. (a) $l = L_0/2$ (b) $l = L_0/5$ (c) $l = L_0/10$ (d) $l = L_0/100$ (e) $l = L_0/\infty$ (f) $l = L_0/\infty$ (g) C^0-NEM

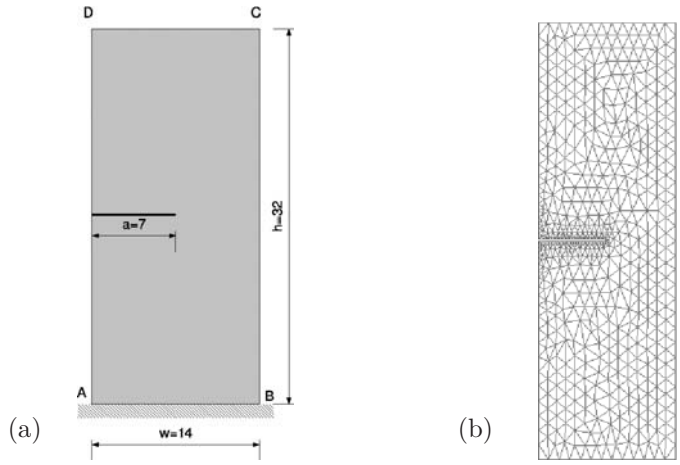

Figure 33: (a) Rectangular specimen with an edge crack. (b) Nodal discretization for the edge crack example.

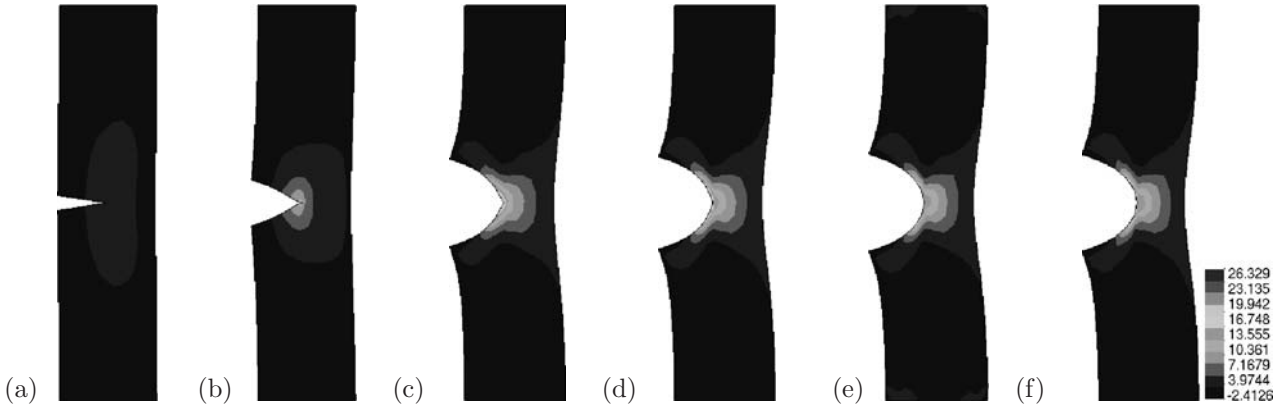

Figure 34: Plot of Cauchy type stresses σ_{11} at various length scales for the edge crack example. (a) $l = L_0/4$ (b) $l = L_0/10$ (c) $l = L_0/50$ (d) $l = L_0/100$ (e) $l = L_0/\infty$ (f) $l = L_0/\infty \quad C^0-$ NEM

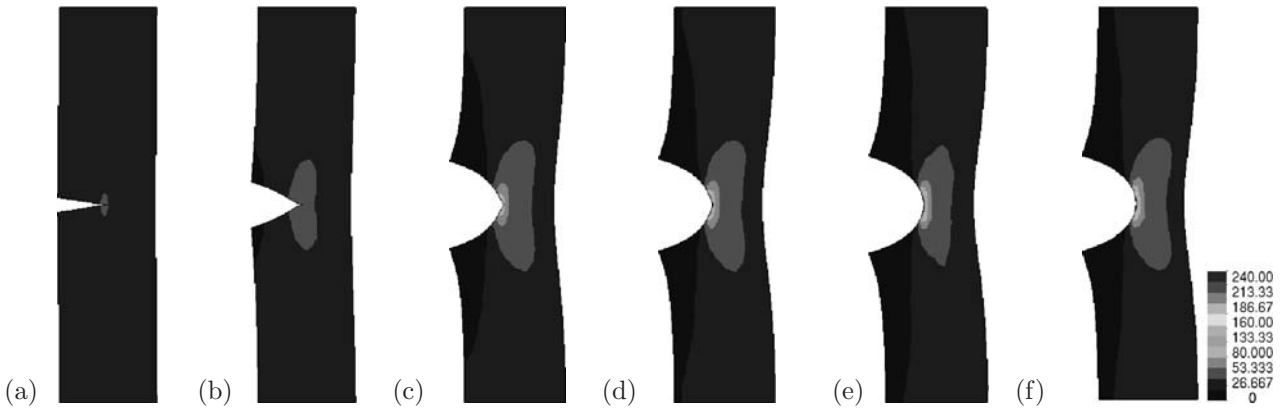

Figure 35: Plot of Cauchy type stresses σ_{22} at various length scales for the edge crack example. (a) $l = L_0/4$ (b) $l = L_0/10$ (c) $l = L_0/50$ (d) $l = L_0/100$ (e) $l = L_0/\infty$ (f) $l = L_0/\infty \quad C^0-$ NEM

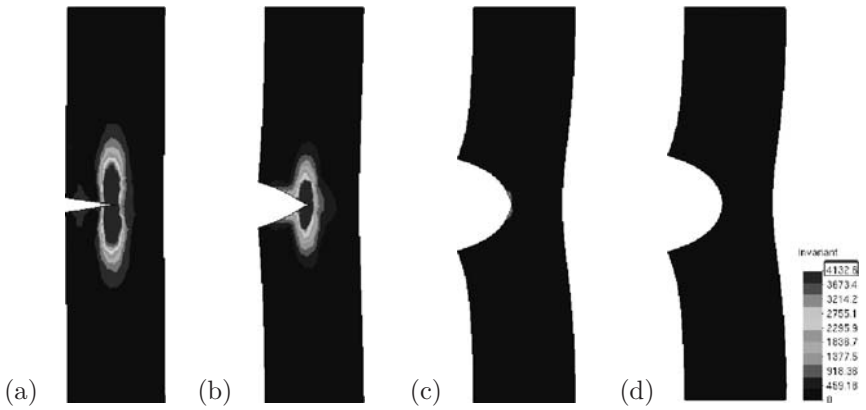

Figure 36: Plot of double stress invariant I_Q at various length scales for the edge crack example. (a) $l = L_0/4$ (b) $l = L_0/10$ (c) $l = L_0/100$ (d) $l = L_0/\infty$

7. Summary and conclusions

In the present work, a gradient continuum formulation is considered. Besides the first gradient, the higher gradients of the displacements are also accounted for in the energy expression. When we consider the second gradient of deformation and ignore even higher gradients, we obtain the strain gradient theory or simply denoted as gradient continuum. From a computational setting the gradient continuum requires no additional degrees of freedom, but results in higher order boundary conditions and has C^1 continuity requirements. To achieve this in the present work an implementation of gradient elasticity using the conformal α-Natural Element Method (α-NEM) has been made. The conformal α-NEM allows the construction of models entirely in terms of nodes and also ensures the linear precision of the interpolant over convex and reasonably also over the non convex boundaries. C^1 natural neighbor interpolants are achieved by a simple transformation of Farin's interpolant, which are obtained by embedding Sibson's natural neighbor coordinates in Bernstein-Bézier surface representations of a cubic simplex. Numerical examples were presented that demonstrated the efficiency and accuracy of the method and the length scale effects. It was observed that the use of gradient elasticity theory removed stress amplification and strain singularity from typical examples of classical elasticity.

Appendix A. Derivation of higher order equilibrium and boundary conditions

Here we give the main steps of the derivation of the higher order equilibrium and boundary conditions. From Eq. (7) we have

$$\delta\Pi = \int\limits_{\mathcal{B}_0} \Big[\boldsymbol{P} : \delta\boldsymbol{F} + \boldsymbol{Q}\vdots\delta\boldsymbol{G} \Big] dV + \delta\Pi^{ext} = 0 \tag{A1}$$

Firstly, the internal potential energy term of the Eq. (A1) is partially integrated (the second term two times) to obtain in a first step

$$\delta\Pi^{\text{int}} = \int\limits_{\mathcal{B}_0} \text{Div}\,(\delta\boldsymbol{\varphi}\cdot\boldsymbol{P})\,\text{dV} - \int\limits_{\mathcal{B}_0} \delta\boldsymbol{\varphi}\cdot\text{Div}\boldsymbol{P}dV + \int\limits_{\mathcal{B}_0} \text{Div}\,(\delta\boldsymbol{F}:\boldsymbol{Q})\,\text{dV} - \int\limits_{\mathcal{B}_0} \delta\boldsymbol{F}:\text{Div}\boldsymbol{Q}dV \tag{A2}$$

and eventually in a second step

$$\begin{aligned}\delta\Pi^{\text{int}} = &\int\limits_{\mathcal{B}_0} \text{Div}\,(\delta\boldsymbol{\varphi}\cdot\boldsymbol{P})\,\text{dV} - \int\limits_{\mathcal{B}_0} \delta\boldsymbol{\varphi}\cdot\text{Div}\boldsymbol{P}dV + \int\limits_{\mathcal{B}_0} \text{Div}\,(\delta\boldsymbol{F}:\boldsymbol{Q})\,\text{dV}\\ &- \int\limits_{\mathcal{B}_0} \text{Div}\,(\delta\boldsymbol{\varphi}\cdot\text{Div}\boldsymbol{Q})\,\text{dV} + \int\limits_{\mathcal{B}_0} \delta\boldsymbol{\varphi}\cdot\text{Div}\,(\text{Div}\boldsymbol{Q})dV\end{aligned} \tag{A3}$$

After application of the Gauss's theorem on the first, third and the fourth terms of Eq. (A4) and grouping of corresponding terms we obtain:

$$\delta\Pi^{int} = \int\limits_{\mathcal{B}_0} \delta\boldsymbol{\varphi}\cdot\text{Div}\,[\text{Div}\,\boldsymbol{Q} - \boldsymbol{P}]dV + \int\limits_{\partial\mathcal{B}_0} \delta\boldsymbol{\varphi}\cdot[\boldsymbol{P} - \text{Div}\boldsymbol{Q}]\cdot\boldsymbol{N}\,dA + \int\limits_{\partial\mathcal{B}_0} \delta\boldsymbol{F}:[\boldsymbol{Q}\cdot\boldsymbol{N}]\,dA \tag{A4}$$

The first and second term of Eq. (A4) contribute to Eq. (9) and Eq. (10), respectively. The variation of $\boldsymbol{F} = \nabla_X\boldsymbol{\varphi}$ in the third term is not independent of the variation of $\boldsymbol{\varphi}$ on $\partial\mathcal{B}_0$, because if $\delta\boldsymbol{\varphi}$ is known on $\partial\mathcal{B}_0$ so is the surface gradient of $\delta\boldsymbol{\varphi}$. Therefore this term cannot directly contribute to the boundary conditions and should be further transformed. Here, the above mentioned material gradient decomposition into normal and tangential parts is used and we obtain:

$$\int\limits_{\partial\mathcal{B}_0} \nabla_X\delta\boldsymbol{\varphi} : [\boldsymbol{Q}\cdot\boldsymbol{N}]\,dA = \int\limits_{\partial\mathcal{B}_0} \nabla_N\delta\boldsymbol{\varphi}\cdot[\boldsymbol{Q}:[\boldsymbol{N}\otimes\boldsymbol{N}]]\,dA + \int\limits_{\partial\mathcal{B}_0} \nabla_X^T\delta\boldsymbol{\varphi}:[\boldsymbol{Q}\cdot\boldsymbol{N}]\,dA \tag{A5}$$

The first term contains independent variations $\nabla_N \delta\boldsymbol{\varphi}$. Integrating the second term by parts we get,

$$\int_{\partial\mathcal{B}_0} \nabla_X^T \delta\boldsymbol{\varphi} : [\boldsymbol{Q}\cdot\boldsymbol{N}]\, dA \equiv \int_{\partial\mathcal{B}_0} [\nabla_X \delta\boldsymbol{\varphi}\cdot\boldsymbol{T}] : [\boldsymbol{Q}\cdot\boldsymbol{N}]\, dA = \int_{\partial\mathcal{B}_0} [\nabla_X (\delta\boldsymbol{\varphi}\cdot[\boldsymbol{Q}\cdot\boldsymbol{N}])] : \boldsymbol{T} dA - \int_{\partial\mathcal{B}_0} [\delta\boldsymbol{\varphi}\cdot\nabla_X (\boldsymbol{Q}\cdot\boldsymbol{N})] : \boldsymbol{T} dA \tag{A6}$$

with $\boldsymbol{T} = [\boldsymbol{I} - \boldsymbol{N}\otimes\boldsymbol{N}]$ the tangent projection to the boundary. Now the first term on the right hand side of Eq. (A6) can be transformed according to the so called surface divergence theorem stemming essentially from the well known Stokes theorem for the closed surface $\partial\mathcal{B}_0$

$$\int_{\partial\mathcal{B}_0} [\nabla_X \boldsymbol{v} : \boldsymbol{T} + K\boldsymbol{v}\cdot\boldsymbol{N}]\, dA = 0 \tag{A7}$$

whereby $K = -\nabla_X \boldsymbol{N} : \boldsymbol{T} = -\nabla_X^T \boldsymbol{N} : \boldsymbol{I}$ is the total curvature of the surface $\partial\mathcal{B}_0$. Application of this transformation leads to the final format of second integral on the right hand side of Eq. (A5) as

$$\int_{\partial\mathcal{B}_0} \nabla_X^T \delta\boldsymbol{\varphi} : [\boldsymbol{Q}\cdot\boldsymbol{N}] dA = \int_{\partial\mathcal{B}_0} \delta\boldsymbol{\varphi}\cdot\boldsymbol{L}(\boldsymbol{Q}\cdot\boldsymbol{N})\, dA \tag{A8}$$

Here the differential operator $\boldsymbol{L}$ is defined as[15]

$$\boldsymbol{L}(\bullet) = -K(\bullet)\cdot\boldsymbol{N} - \nabla_X^T(\bullet) : \boldsymbol{I} \tag{A9}$$

Using these expressions the variation of the total internal potential energy can thus be written as

$$\delta\Pi^{int} = \int_{\mathcal{B}_0} \delta\boldsymbol{\varphi}\cdot \mathrm{Div}\,[\mathrm{Div}\boldsymbol{Q} - \boldsymbol{P}] dV + \int_{\partial\mathcal{B}_0} \delta\boldsymbol{\varphi}\cdot[[\boldsymbol{P} - \mathrm{Div}\boldsymbol{Q}]\cdot\boldsymbol{N} + \boldsymbol{L}(\boldsymbol{Q}\cdot\boldsymbol{N})]\, dA + \int_{\partial\mathcal{B}_\prime} \nabla_N \delta\boldsymbol{\varphi}\cdot[\boldsymbol{Q} : [\boldsymbol{N}\otimes\boldsymbol{N}]]\, dA \tag{A10}$$

Each integral in this expression contains only independent variations and therefore the equilibrium and boundary conditions can be written in the form given in Eq. (9) to Eq. (12).

References

Amanatdou, E. and Aravas, A. (2002). Mixed finite element formulations of strain-gradient elasticity problems, *Computer Methods in Applied Mechanics and Engineering* **191**, pp. 1723–1751.

Askes, H. and Aifantis, E. C. (2002). Numerical modeling of size effects with gradient elasticity-formulation meshless discretization and examples, *International Journal of Fracture* **117**, pp. 347–358.

Belytschko, T., Lu, Y. Y. and Gu, L. (1994). Element free Galerkin methods, *International Journal for Numerical Methods in Engineering* **37**, pp. 229–256.

Braun, J. and Sambridge, M. S. (1995). A numerical method for solving partial differential equations on highly irregular evolving grids, *Nature* **376**, 1, pp. 655–660.

[15] The gradient operator can be decomposed in to normal and tangential parts according to the following rule : $\nabla_X(\bullet) = [\nabla_X(\bullet)\cdot\boldsymbol{N}]\,\boldsymbol{N} + \nabla_X(\bullet)\cdot[\boldsymbol{I} - \boldsymbol{N}\otimes\boldsymbol{N}]$, whereby $\boldsymbol{N}$ denotes the material surface normal vector.

Cazals, F., Giesen, J., Pauly, M. and Zomorodian, A. (2006). The conformal alpha shape filtration, *Visual Computations* **22**, pp. 531–540.

Cueto, E., Doblaré, M. and Calvo, B. (2002). Modelling three dimensional piece wise homogeneous domains using the α-shape based natural element method, *International Journal for Numerical Methods in Engineering* **54**, pp. 871–897.

Cueto, E., Doblaré, M. and Gracia, L. (2000). Imposing essential boundary conditions in the natural element method by means of density scaled α-shapes, *International Journal for Numerical Methods in Engineering* **49**, pp. 519–546.

Edelsbrunner, H., Kirkpatrick, D. and Seidel, R. (1983). On the shape of a set of points in plane, *IEEE Transactions on information theory.* **29**, 4, pp. 551–559.

Edelsbrunner, H. and Mucke, E. (1994). Three dimensional alpha shapes, *ACM transactions on graphics* **13**, 1, pp. 43–72.

Eringen, A. C. (1964). Mechanics of micromorphic materials, in H. Gorliter (ed.), *Proc. 11th Int. Congress of Appl. Mech.*, pp. 131–138.

Eringen, A. C. (1970). Balance laws of micromorphic mechanics, *International Journal of Engineering Science* **85**, pp. 819–828.

Eringen, A. C. (1992). Balance laws of micromorphic continuua revisited, *International Journal of Engineering Science* **30**, 6, pp. 805–810.

Eringen, A. C. (1998). Microcontinuum field theories-1. foundations and solids, *Springer-Verlag, Newyork, Inc.* .

Farin, R. (1985). Curves and surfaces for computer aided geometric design, *Computer science and Scientific computing, Academic press,London , UK* **4th edition**, pp. 19–27.

Farin, R. (1986). Triangular Bernstein Bézier patches, *Computer Aided Geometirc Design* **7**, pp. 83–127.

Farin, R. (1990). Surfaces over Dirichlet tesellations, *Computer Aided Geometric Design* **7**, pp. 281–292.

Fleck, N. and Hutchinson, J. (1996). Strain gradient plasticity, *Adv. app.Mech* **33**.

Hirschberger, B. and Steinmann, P. (2007). On deformation and configurational mechanics of micromorphic hyperelasticity-theory and computations, *Computer Methods in Applied Mechanics and Engineering* **40**, 4, pp. 4027 – 4044.

Kirchner, N. and Steinmann, P. (2005). A unifying treatise on variational principles of gradient and micromorphic continuaa, *Philosophical Magazine* **85**, 33-35, pp. 3875–3895.

Kirchner, N. and Steinmann, P. (2007). On material setting of gradient hyperelasticity, *Mathematics and Mechanics of Solids* **12**, 5, pp. 559–580.

Kouznetsova, V. G. (2002). Computational homogenization for the multiscale analysis of multipahse materials, *PhD, thesis, Technische Universiteit, Eindhoven* .

Kouznetsova, V. G., Geers, M. G. D. and Brekelmans, W. A. M. (2004). Multiscale second order computational homogenization of multiphase materials: A nested finite element solution strategy, *Computer Methods in Applied Mechanics and Engineering* **193**, pp. 5525–5550.

Mindlin, D. and Tiersten, H. F. (1962). Effects of couple stress in linear elasticity, *Arc. Rat. Mech. Anal.* **11**, pp. 415–448.

Mindlin, D. and Tiersten, H. F. (1964). Microstructure in linear elasticity, *Arc. Rat. Mech. Anal.* **16**, pp. 51–78.

Mindlin, R. D. (1965). Second gradient in strain and surface tension in linear elasticity, *Int. J. of Solids and Structures* **1**, 3, pp. 417–438.

Sambridge, M. S., Braun, J. and McQueen, H. (1995). Geophysical parametrization and interpolation of irregular data using natural neighbours, *Geophys. J. Int.* **122**, 1, pp. 837–857.

Shu, J., King, W. and Fleck, N. (1999). Finite elements for materials with strain gradient effects, *International Journal for Numerical Methods in Engineering* **44**, pp. 373–391.

Sibson, R. (1980). A vector identity for the Dirichlet tessellation, *Mathematical Proceedings of Cambridge Philosophical Society* **87**, pp. 151–155.

Sibson, R. (1981). A brief description of natural neighbor interpolation, in V. Barnett (ed.), *Interpreting Multivariate Data* (John Wiley, Chichester), pp. 21–36.

Stogner, R. H. and Carey, G. F. (2007). C^1 macro elements in adaptive finite element methods, *International Journal of numerical methods in engineering* **70**, pp. 1076–1095.

Sukumar, N. and Moran, B. (1999). C^1 natural neighbour interpolant for partial differential equations, *International Journal for Numerical Methods in Engineering* **15**, 1, pp. 417–447.

Sukumar, N., Moran, B. and Belytschko, T. (1998). The natural element method in solid mechanics, *International Journal for Numerical Methods in Engineering* **43**, 1, pp. 839–887.

Sunyk, R. and Steinmann, P. (2003). On higher gradients in continuum atomistic modelling, *International Journal of Solids and Structures* **40**, pp. 6877–6896.

Tang, Z., Shen, S. and Atluri, S. N. (2003). Analysis of materials with strain gradient effects: A mesh less local petrov Galerkin approach, with nodal displacements only, *Computer modelling in Engineering Sciences* **4**, 1, pp. 177–196.

Toupin, R. A. (1962). Elastic materials with couple stress, *Arc. Rat. Mech. Anal.* **11**, pp. 385–414.